SRON
Netherlands Institute for Space Research

esa

ESA STUDY CONTRACT REPORT – SPECIMEN

No ESA Study Contract Report will be accepted unless this sheet is inserted at the beginning of each volume of the Report.

ESA Contract No: 4000125587/18/I-NS	SUBJECT: The Living Planet Fellowship Water vapour Isotopologues from TROPOMI (WIFT)	CONTRACTOR: SRON
* ESA CR( )No:	No. of Volumes: 6 This is Volume No: 6	CONTRACTOR'S REFERENCE: SRON-EARTH-PRP-2018-001

ABSTRACT:
The role of atmospheric water vapour in the hydrological cycle, the atmospheric circulation, and the radiation and energy budgets is largely uncertain. Improving knowledge on these is one of the key challenges in atmospheric sciences and of great importance for projections of climate change. Measurements of water isotopologues provide information about the history of a sampled air parcel due to isotopic fractionation during evaporation and condensation and so give significant constraints for the processes involved. Global observations are especially useful for constraining general circulation models, but to date no satellite data set with high sensitivity in the lowermost troposphere (where most water vapour resides) and decent spatial and temporal resolution and data quality is available. The new Tropospheric Monitoring Instrument (TROPOMI) aboard the Sentinel 5 Precursor satellite is expected to be a 'game-changer', as it measures sunlight reflected by Earth's atmosphere in the shortwave infrared spectral range with unprecedented spatial resolution up to 7 km × 7 km, daily global coverage, and high radiometric performance. The subject of this project is to exploit these measurements to retrieve the water vapour isotopologues $H_2{}^{16}O$, HDO and, if possible, $H_2{}^{18}O$. To this end, the SICOR retrieval algorithm suite, which has high software maturity, is employed. After setting up a processing pipeline at a high performance computing infrastructure, results will be validated against ground-based observations from the Total Carbon Column Observing Network (TCCON) and in-situ measurements by the In-Service Aircraft for a Global Observing System (IAGOS) Civil Aircraft for the Regular Investigation of the atmosphere Based on an Instrument Container (CARIBIC) project. Should recent data from the Multi-platform remote Sensing of Isotopologues for investigating the Cycle of Atmospheric water (MUSICA) project become available, these will also be used for validation. The influence of state-of-the-art molecular water vapour spectroscopy on the data product will be investigated. Moreover, the feasibility to infer the $H_2{}^{18}O$ isotopologue from TROPOMI measurements will be assessed. In this context, the spectral window will be optimised to minimise cross-dependencies between different isotopologues. Finally, the maturity and use of the new data product will be demonstrated. First, it will be compared to simulations with an isotope-enable global circulation model. The topic of the following investigation depends on the outcome of the feasibility study. In case the deuterium excess parameter can be obtained with sufficient accuracy, water vapour originating from combustion shall be studied on city scale. Alternatively, the role of evapotranspiration on the isotopic composition ($HDO/H_2{}^{16}O$) in dependence of land usage will be examined. The outcome of this project will be an additional mature data product in ESA's portfolio from the Sentinel missions.

Names of authors:
Andreas Schneider

** NAME OF ESA STUDY MANAGER:	** ESA BUDGET HEADING:
Diego Fernandez DIV: DIRECTORATE:	

* Sections to be completed by ESA
** Information to be provided by ESA Study Manager

FINAL REPORT

Water vapour Isotopologues from TROPOMI (WIFT)

Andreas Schneider
SRON Netherlands Institute for Space Research

Prepared by	Andreas Schneider
Approved by	Jochen Landgraf
Reference	FR_WIFT
Date of Issue	2021-05-25

Jochen Landgraf

Digitally signed by Jochen Landgraf
Date: 2021.05.26 21:18:15 +02'00'

1 Executive Summary

This document describes the work and results of the Living Planet Fellowship "Water vapour Isotopologues from TROPOMI" (WIFT). The aim of the project was to create a new data product of water vapour isotopologue column densities from short-wave infrared measurements by the Tropospheric Monitoring Instrument (TROPOMI) and use the new data set in a science study in the later part of the project.

First, a retrieval using a profile-scaling approach with a radiative transfer model neglecting scattering has been set up. Such a retrieval requires strict clear-sky filtering, which is performed using a collocated cloud data product from the Visible Infrared Imaging Radiometer Suite (VIIRS).

Validation is important for a new data product. Currently, only ground-based Fourier transform infrared measurements by the Total Carbon Column Observing Network (TCCON) are available as reference with recent data and sufficient coverage. The TCCON HDO data product unexpectedly turned out to be biased. This can clearly be seen by comparing TCCON δD with ground-based measurements by the project Multi-platform remote Sensing of Isotopologues for investigating the Cycle of Atmospheric water (MUSICA) at stations in both networks for a period where MUSICA data are available. As MUSICA δD is validated with aircraft measurements but TCCON HDO is currently not verified, an overall correction of recent TCCON HDO data is derived by scaling TCCON HDO columns to match TCCON δD to MUSICA δD for the common time period.

The overall validation of the scattering product with the corrected TCCON measurements yields good agreement. The average bias is $(-0.3 \pm 1) \times 10^{21}$ molec cm^{-2} or (-0.7 ± 3.5) % in H_2O and $(-0.9 \pm 3) \times 10^{17}$ molec cm^{-2} or (-1.3 ± 3.3) % in HDO, which corresponds to a bias of (-7 ± 13) ‰ or (3.8 ± 6.5) % in a posteriori δD. Low latitude stations have biases in δD ranging between about -30 ‰ and $+15$ ‰, while at high latitude stations the bias can be as high as -45 ‰ to -60 ‰. At high latitudes retrievals are generally challenging due to high solar zenith angles and low albedos which lead to low signal-to-noise ratios.

The effect of using different scattering cross-sections has been studied. Compared to the proposal, cross sections have been updated to HITRAN 2016 which significantly improves fitting quality as well as validation. Furthermore, runs have been performed with cross-sections for single absorbers or all absorbers changed from HITRAN 2016 to Scientific Exploitation of Operational Missions (SEOM) Improved Atmospheric Spectroscopy Databases (IAS). SEOM-IAS cross-sections especially of CH_4 improve the fit quality but worsen the validation with corrected TCCON measurements. Since a good validation is considered more important than improvements in fit quality, the decision is to continue using HITRAN 2016.

An experiment to also fit the isotopologue $H_2{}^{18}O$ has been performed with the non-scattering retrieval. Reference data is available at two stations only. The quality of inferred $\delta^{18}O$ is bad with a Pearson correlation of -0.17 in the best case. The signal appears to be too weak to infer $H_2{}^{18}O$ with the required precision.

To extend data coverage to scenes with low clouds, a second retrieval has been set up which employs a forward model that does account for scattering and fits effective cloud parameters additionally to the trace gases. Unexpectedly, an approach to fit cloud parameters simultaneously to the trace gases similar to the CO product turned out not to work after many experiments with different setups and different cloud models. Finally, the problem has been solved by fitting cloud parameters in a different spectral window in the SWIR range and taking the result over to the final fit of the trace gases. The new retrieval tremendously enhances coverage, not only due to the inclusion of cloudy scenes which particularly enables data over oceans, but also due to relaxed filtering for clear-sky scenes compared to the non-scattering retrieval. The validation of the new retrieval proves good performance. The bias for clear-sky scenes is $(0.9 \pm 2) \times 10^{21}$ molec cm^{-2} or (-2.0 ± 5.1) % in H_2O, $(0.7 \pm 4) \times 10^{17}$ molec cm^{-2} or (0.1 ± 3.9) % in HDO, and (-15 ± 16) ‰ or (8.5 ± 6.7) % in a posteriori δD. For cloudy scenes, the bias is $(3 \pm 3) \times 10^{21}$ molec cm^{-2} or (7.9 ± 6.4) % in H_2O, $(6 \pm 7) \times 10^{17}$ molec cm^{-2} or (4.9 ± 5.4) % in HDO, and (-20 ± 11) ‰ or (10 ± 5.7) % in a posteriori δD.

With each data set, a case study based on single overpass data has been performed in collaboration with Franziska Aemisegger (ETH Zürich). With the non-scattering retrieval, a blocking anticyclone on 30th July 2018 has been studied. Subsiding air masses in the core of the anticyclone led to isotopic depletion of the column by bringing depleted upper-tropospheric air to lower levels. Divergent winds near the surface exported freshly evaporated more enriched air to the edge of the blocking. With the scattering retrieval, a cold air outbreak in January 2020 has been analysed with data over cloudy scenes over the Atlantic Ocean. Retrievals from consecutive days nicely show the transport of depleted continental air from high to subtropical latitudes. These case studies demonstrate the data quality of the new data sets and the new possibilities for isotopological studies.

To sum up, two new datasets have been released and published within this fellowship, namely the first data set of clear-sky H_2O and HDO observations from TROPOMI and the first data set of H_2O and HDO observations over cloudy and clear-sky scenes from TROPOMI. Each dataset is validated and demonstrated with a case study using single overpass data.

2 Objectives and work plan

The main objective of this project has been to create a water vapour isotopologue column density data set from TROPOMI short-wave infrared measurements with a maturity equivalent to an operational status, which is validated against ground-based and in situ measurements. Retrieved isotopologues are H_2O and HDO; a sub-objective has been to check if the additional retrieval of $H_2{}^{18}O$ is feasible. The second objective has been to advance knowledge of the hydrological cycle in a dedicated science study using the newly created data set, with the topic dependent on the outcome of the feasibility study to retrieve $H_2{}^{18}O$ with sufficient accuracy.

These objectives have been translated to the work packages defined in Tab. 1. Figure 1 shows the time plan at the beginning of the project. The first goal has been creating a data set of the isotopologues HDO and H_2O simultaneously retrieved as independent trace gases from TROPOMI observations (WP 1). The retrieval employs a profile-scaling approach with the Shortwave Infrared CO Retrieval (SICOR) algorithm. WP 1 contains two sub-goals. First, a clear-sky retrieval has been set up, which uses a forward model that ignores scattering and is thus termed non-scattering retrieval hereafter. Secondly, the SICOR algorithm can also infer, in addition to the atmospheric trace gas columns, effective cloud parameters (optical depth and height of a scattering layer) from the CH_4 absorptions of the measurement describing the light path in the shortwave infrared spectral range. This employs a forward model which accounts for scattering and is used to retrieve over cloudy and clear-sky scenes. WP 2 assesses the impact of updated scattering cross-section tables, such as the ones measured within ESA's Scientific Exploitation of Operational Missions (SEOM) Improved Atmospheric Spectroscopy Databases (IAS) project.

WP 4 evaluates the feasibility of retrieving the isotopologue $H_2{}^{18}O$ as independent absorber in addition to $HD^{16}O$ and $H_2{}^{16}O$. The benchmark for the evaluation is the validation of a posteriori calculated δD, δ^{18}O, and d-excess. Due to the

Table 1: Description of work packages.

WP	Work package name	Preliminaries	Deliverables	Time
1	Create TROPOMI H_2O/HDO data product	Access to TROPOMI and meteo data, access to SICOR, access to supercomputing facility	Validated H_2O/HDO data product, set up processing pipelines	6 mon
1.1	Product for clear-sky scenes			
1.2	Product for cloudy and clear-sky scenes			
2	Assess updated spectroscopy	Access to spectroscopy line list		2 mon
3	Write technical report 1		Report	1 week
4	Feasibility study of $H_2{}^{18}O$ retrieval	TROPOMI water vapour isotopologue retrievals are set up	Evaluation of accuracy of inferred $H_2{}^{18}O$, δ^{18}O, and d-excess	6 mon
5	Write mid-term report		Report	2 weeks
6	Science study	Decision on $H_2{}^{18}O$ retrieval (MS1), global data set of H_2O, HDO, and in case of option 6.1 $H_2{}^{18}O$ with sufficient accuracy in a posteriori d-excess	Publication of results	8 mon
7	Write technical report 2		Report	1 week
8	Write final report		Report	3 weeks

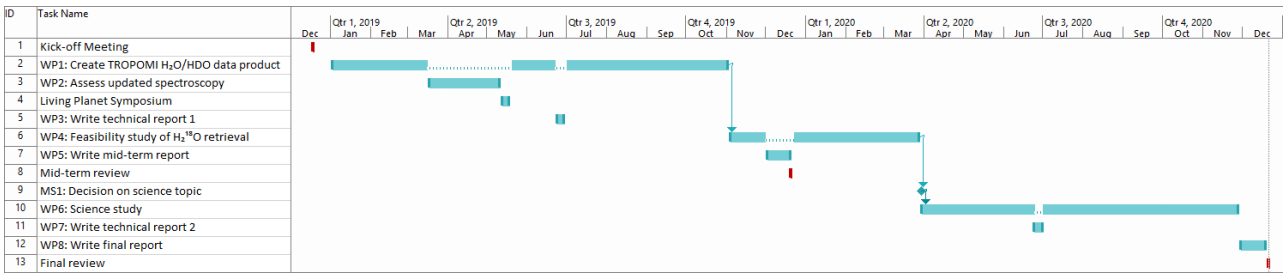

Figure 1: Gantt chart of the time plan at the beginning of the project.

slope of 8 in the Global Meteoric Water Line (GMWL), δ^{18}O has to be inferred with a much better accuracy than δD for a meaningful estimation of d-excess, which is challenging. Finally, WP 6 employs the actual use of the new data sets in scientific case studies.

Work packages 3, 5, 7 and 8 correspond to the compulsory reports. Bimonthly progress reports are not separate work packages but are included in the topical work packages.

3 Work performed

3.1 Scientific context

Atmospheric moisture strongly controls Earth's radiative budget and transports energy via latent heat, e.g. from low to high latitudes. Uncertainties in the quantification of these two effects are still large and represent one of the key uncertainties in current climate prediction [Stevens and Bony, 2013]. Isotopologues of water offer further insights into the water cycle due to fractionation processes on phase changes. That provides additional constraints for models and thus valuable insights for their improvement. The application of isotopic effects to this end requires observations on global scale and with a long-term perspective, whereto satellite observations from space are most promising [Rast et al., 2014].

Water vapour isotopologues are retrieved from satellite either in the thermal infrared or the short-wave infrared spectral range. The former are insensitive to the boundary layer, the region where most water vapour resides. The latter, at the beginning of the project, lacked data quality, spatial resolution, or geographic coverage. For example, GOSAT has a sparse geographical coverage with ground pixels separated by typically 158 km but with a spatial resolution of 10 km. TROPOMI promised to overcome these shortcomings with short-wave infrared measurements with good signal-to-noise ratio, high spatial resolution and daily global coverage, but water vapour isotopologues had not yet been retrieved from TROPOMI.

Isotopological abundance variations are often described by the so-called δ notation which denotes the relative difference of the ratio of the heavy and the light isotopologue, $R_{\mathrm{HDO}} = c_{\mathrm{HDO}}/c_{\mathrm{H_2O}}$, to the standard abundance ratio of Vienna Standard Mean Ocean Water (VSMOW) $R_{\mathrm{HDO,std}} = 3.1152 \times 10^{-4}$, i. e.

$$\delta\mathrm{D} = \frac{R_{\mathrm{HDO}} - R_{\mathrm{HDO,std}}}{R_{\mathrm{HDO,std}}} \tag{1}$$

[Craig, 1961b, Hagemann et al., 1970]. This nomenclature is also used herein.

3.2 Methods

3.2.1 General retrieval method

The retrieval employs a profile-scaling approach with the Shortwave Infrared CO Retrieval (SICOR) algorithm, which is described in detail by Scheepmaker et al. [2016], Landgraf et al. [2016] and Borsdorff et al. [2014].

The algorithm supports several forward models. The simplest one ignores scattering; a retrieval with this model is termed non-scattering retrieval. An alternative forward model accounts for scattering using the Practical Improved Flux Method [PIFM, Zdunkowski et al., 1980]. It assumes a single scattering layer with a triangular height profile in extinction coefficient centred at cloud centre height h with a geometrical half-width d and a cloud optical thickness of τ. A third forward model is termed elevated reflecting surface (ERS) and basically assumes a partial coverage (determined by a cloud fraction f) with a non-transparent thin layer with cloud albedo a and cloud height h. The idea for the latter two models is to infer the effective cloud parameters, additionally to the trace gases, from deviations of the retrieved methane column to the prior, as these are supposed to originate from light path modifications by scatterers.

The target trace gases H_2O and HDO are fitted together with the interfering species CH_4 and CO and a Lambertian surface albedo in the spectral window from 2354.0 nm to 2380.5 nm [Scheepmaker et al., 2016]. The isotopologue $H_2{}^{18}O$ is included in the forward model but not fitted. An experiment to additionally fit $H_2{}^{18}O$ is described below. Scattering cross-sections are taken from the high-resolution transmission molecular absorption database (HITRAN) 2016 release [Gordon et al., 2017]. Alternatives are considered in an experiment described below.

A priori profiles of water vapour are adapted from the European Centre for Medium-Range Weather Forecasts (ECMWF) analysis product. Since the ECMWF data product does not distinguish individual isotopologues, H_2O, HDO and $H_2{}^{18}O$ profiles are obtained from the water vapour profile by scaling it with the respective average relative natural abundances. That implicitly corresponds to a prior of δD of 0 ‰. A case study for high-altitude stations in Sec. 3.4.5 alternatively uses HDO prior profiles computed from H_2O profiles via an assumed more realistic δD profile which linearly decreases from -100 ‰ at the surface to -600 ‰ at 15 km altitude followed by a linear increase to -400 ‰ at the top of the atmosphere

as used by Scheepmaker et al. [2016] for their simulated measurements. From this δD profile, a δ^{18}O profile is computed via the global meteoric water line

$$\delta\mathrm{D} = 8\,\delta^{18}\mathrm{O} + 10\,‰ \tag{2}$$

[Craig, 1961a] and used to obtain the $H_2{}^{18}O$ prior profile from the H_2O profile. A priori profiles of CH_4 and CO are taken from TM5 simulations [Krol et al., 2005].

3.2.2 Clear-sky retrieval

Since the forward model ignores scattering, strict filtering for clear-sky scenes is necessary. To this end, collocated measurements from the Visible Infrared Imaging Radiometer Suite (VIIRS) instrument onboard the Suomi National Polar-orbiting Partnership (S-NPP) satellite, which flies in formation with S5P, are used [Siddans, 2016]. The cloud cover threshold is 1 % for both the inner field of view and the outer field of view. Moreover, soundings with a high aerosol load are filtered out by a two-band filter as introduced by Scheepmaker et al. [2016] and Hu et al. [2018], which in the present configuration requires that the ratio of retrieved methane in bands with weak and strong absorption (2310–2315 and 2363–2373 nm, respectively) is between 0.94 and 1.06. Furthermore, scenes with a solar zenith angle greater than 75° are discarded because they are prone to errors due to more scattering and diffraction effects, which are not covered well by the forward model, and due to typically low radiances, meaning low signal-to-noise ratios. Table 2 summarises all filters.

Table 2: Filters for the non-scattering retrieval.

Quantity	Filter
VIIRS cloud fraction ifov	$f_{\mathrm{ifov}} \leq 0.01$
VIIRS cloud fraction ofova	$f_{\mathrm{ofova}} \leq 0.01$
VIIRS cloud fraction ofovb	$f_{\mathrm{ofovb}} \leq 0.01$
VIIRS cloud fraction ofovc	$f_{\mathrm{ofovc}} \leq 0.01$
Two-band CH_4	$0.94 \leq \frac{c_{\mathrm{CH_4,weak}}}{c_{\mathrm{CH_4,strong}}} \leq 1.06$
Solar zenith angle	$\varphi \leq 70°$

An exemplary spectral fit and the resulting residuals (which are defined as measured minus modelled radiances) are shown in Fig. 2. The root-mean-square (rms) residual (cyan horizontal line in Fig. 2b) is in the order of the rms uncertainty of the radiance (purple horizontal line in Fig. 2b).

The sensitivity of a retrieved column to changes in a given altitudinal region is described by the column averaging kernel [Rodgers, 2000]. The ideal averaging kernel is unity at all altitudes, but in practice the sensitivity changes with height. Figure 3 depicts examples of column averaging kernels for different solar zenith angles. The sensitivity for the two isotopologues are significantly different. For H_2O, the highest sensitivity is in the lowest layer (where most water vapour typically resides) and decreases with increasing altitude. The sensitivity in the stratosphere is small; however, the amount of water vapour in this altitudinal region is very small and contributes little to the total column. The sensitivity of HDO does not deviate as much from unity as that of H_2O. In the lower troposphere it increases slightly with increasing altitude before reaching a maximum depending on the solar zenith angle, above which it decreases. The differences in the column averaging kernel are due to the different absorption strengths of the two isotopologues and mean that a posteriori δD is sensitive to the profile shapes, particularly of the main isotopologue H_2O; this is due to the fact that the averaging kernel for H_2O deviates considerably from unity at higher altitudes.

3.2.3 Correction of reference data for validation

Two HDO and H_2O data products from ground-based Fourier transform infrared (FTIR) observations are available: The one by the Total Carbon Column Observing Network [TCCON, Wunch et al., 2011], and the one by the project Multi-platform remote Sensing of Isotopologues for investigating the Cycle of Atmospheric water [MUSICA, Schneider et al., 2016, Barthlott et al., 2017], which uses spectra measured within the Network for the Detection of Atmospheric Composition Change [NDACC, De Mazière et al., 2018]. Two different MUSICA-NDACC products exist: firstly the direct retrieval output, called type 1 product, and secondly an a posteriori processed output that reports the optimal estimation of (H_2O, δD) pairs, called type 2 product. Here, the type 2 product is used because it is recommended for isotopologue analyses [Barthlott et al., 2017].

Seven stations are in both networks. They are listed in Tab. 3. This allows to compare the TCCON and NDACC-MUSICA (here type 2) data products, which reveals an unexpectedly large differences in all three quantities H_2O, HDO

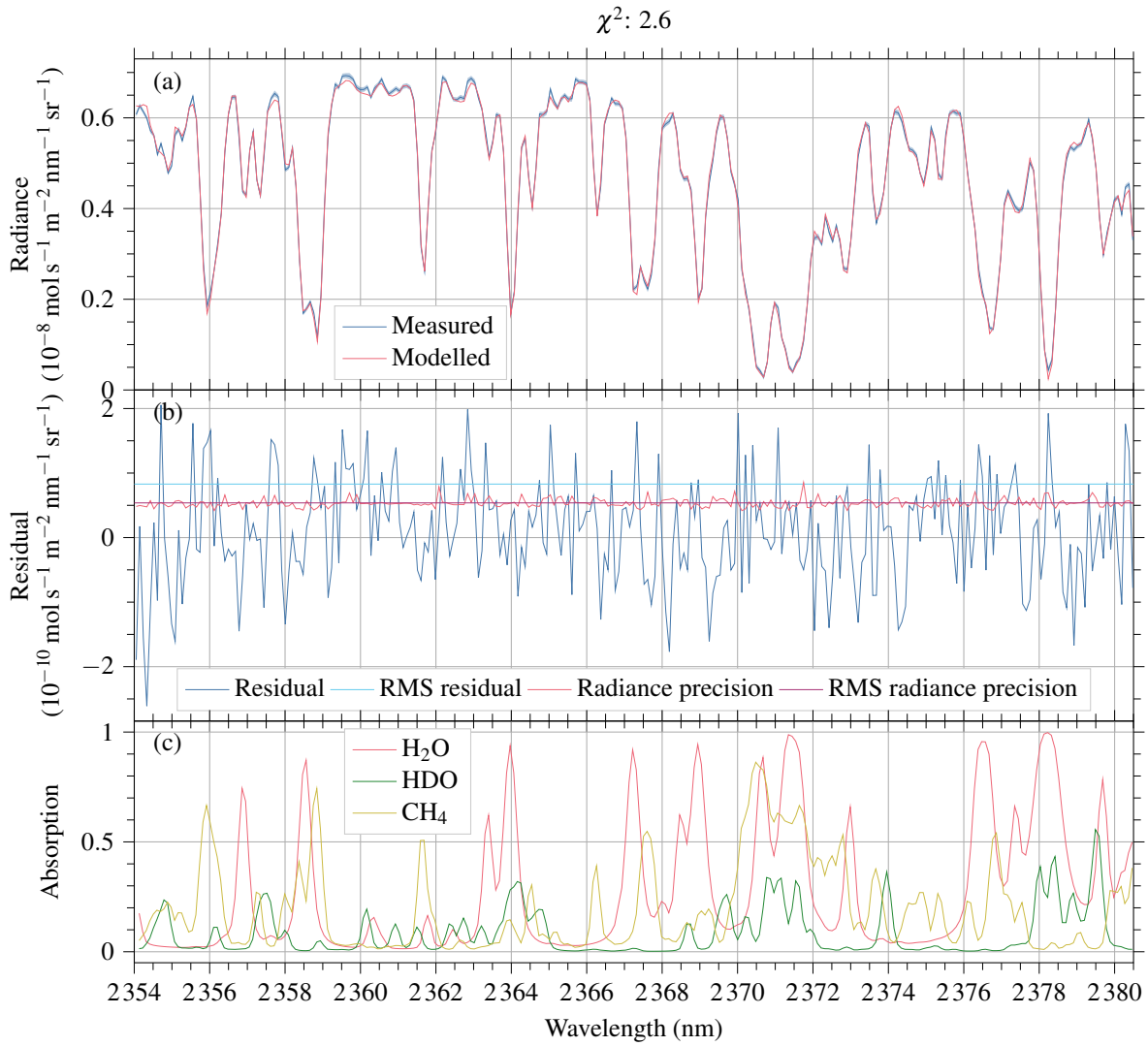

Figure 2: **(a)** Measured radiance (blue) with its precision (light blue shading) and the spectral fit (red) for ground pixel 149 129 in orbit 3969 located near Wollongong, Australia on 20 July 2018. **(b)** Corresponding residuals (defined as measured minus modelled radiances, in blue) and its root mean square (rms, in cyan), precision of the radiance (in red) and its rms (in purple). **(c)** Simulated absorption by H_2O (red), HDO (green) and CH_4 (yellow).

Table 3: List of ground stations used for the derivation of the FTIR correction.

Station	Lat.	Lon.	Altitude	MUSICA available from/to	TCCON available from/to	TCCON reference
Eureka	80° N	86° W	610 m	01 Aug 2006 – 01 Sep 2014	24 Jul 2010 – 28 Mar 2018	Strong et al. [2019]
Ny Ålesund	79° N	12° E	20 m	08 Apr 2005 – 27 Aug 2014	28 Mar 2006 – 17 Sep 2017	Notholt et al. [2019b]
Bremen	53° N	9° E	30 m	21 Jul 2004 – 14 Oct 2014	15 Jan 2007 – 29 Dec 2017	Notholt et al. [2019a]
Karlsruhe	49° N	8° E	110 m	17 Apr 2010 – 15 Dec 2014[1]	19 Apr 2010 – 30 Sep 2018[1]	Hase et al. [2015]
Izaña	28° N	17° W	2370 m	18 Jun 2001 – 26 Dec 2014[2]	18 May 2007 – 18 Sep 2018[2]	Blumenstock et al. [201
Wollongong	34° S	151° E	30 m	07 Aug 2007 – 09 Sep 2014	25 Jun 2008 – 13 Sep 2017	Griffith et al. [2014b]
Lauder	45° S	170° E	370 m	06 Sep 1997 – 30 Aug 2014	02 Feb 2010 – 04 Jul 2018	Sherlock et al. [2014]

1 later extended to 12 Sep 2019 and 25 Jun 2020, respectively
2 later extended to 25 Sep 2019 and 30 Jun 2020, respectively

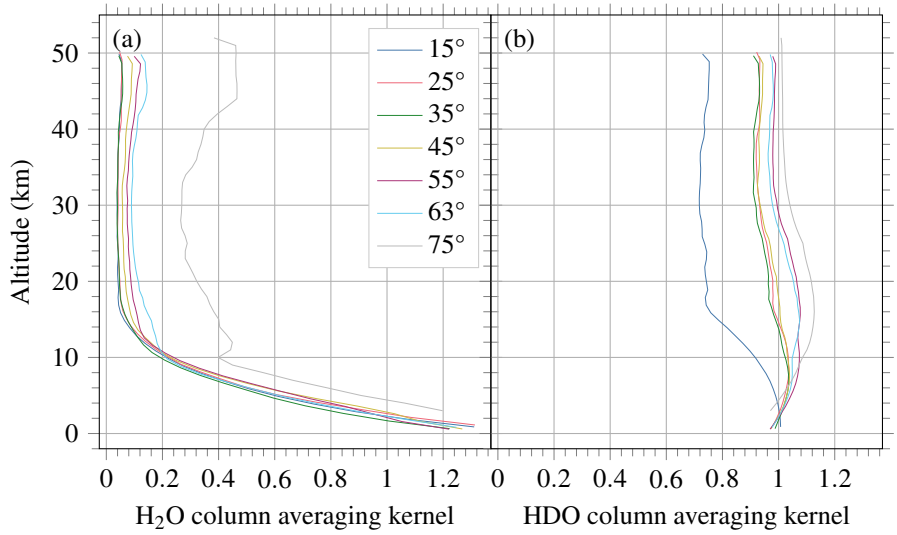

Figure 3: Examples of column averaging kernels for **(a)** H_2O and **(b)** HDO for different solar zenith angles in orbit 4924 on 25 September 2018.

and a posteriori δD. The bias in δD is on average 58 ‰ (corresponding to a mean relative difference of −30 %) when collocating with a maximal time difference of one hour. An example for Wollongong is plotted in Fig. 4. MUSICA is explicitly created for isotopologue studies, and δD profiles have been validated against aircraft measurements in an altitude range of 2–7 km during a dedicated campaign in summer 2013 [Schneider et al., 2015, Dyroff et al., 2015, Schneider et al., 2016]. However, data for most stations is only available until 2014. Recently in 2020, new MUSICA data with temporal overlap with the TROPOMI mission have become available for three stations (Karlsruhe, Kiruna and Izaña), but the small number of stations still compromises globally valid validation studies. TCCON H_2O total columns are calibrated with in situ measurements (mainly radiosondes); a so-called aircraft correction factor of 1.0183 is applied to match the reference [Wunch et al., 2015]. However, TCCON HDO is currently not verified and so no correction factor

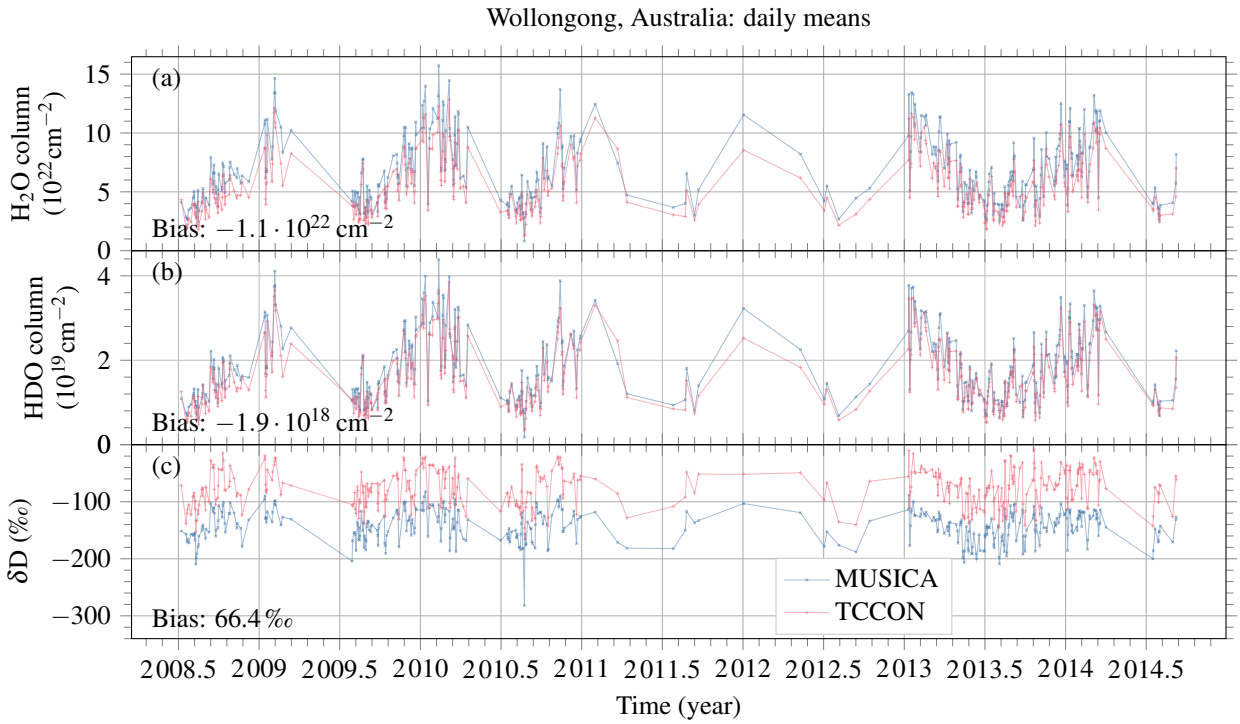

Figure 4: Time series of daily averages of H_2O **(a)**, HDO **(b)** and a postiori δD **(c)** of the NDACC-MUSICA type 2 (blue crosses) and TCCON (red pluses) data products at Wollongong, Australia. The bias in δD without daily averaging is 65.8 ‰ (−47.4 %).

is applied to it. Thus it is assumed that TCCON HDO has to be corrected.

In order to correct for the discrepancy, the idea is to scale TCCON HDO to match MUSICA δD. Scaling HDO with a factor a, i. e. $c_{\mathrm{HDO}} \mapsto a\,c_{\mathrm{HDO}}$, is equivalent to the linear transformation

$$\delta\mathrm{D} \mapsto a\,\delta\mathrm{D} + a - 1 \tag{3}$$

in δD. Figure 5a depicts a correlation histogram of TCCON δD vs. MUSICA δD for the station Wollongong. Here, the relation between MUSICA and TCCON is to a good degree described by a simple scaling of the column. The result of a fit of Eq. (3) to the data is plotted as blue line, giving the scaling factor for the TCCON HDO column. The bar chart in Fig. 5c visualises fit results for all stations in both networks. It shows that the correction factor does not change much between stations. The large difference in fit error is mostly due to the large difference in the amount of data (Fig. 5b).

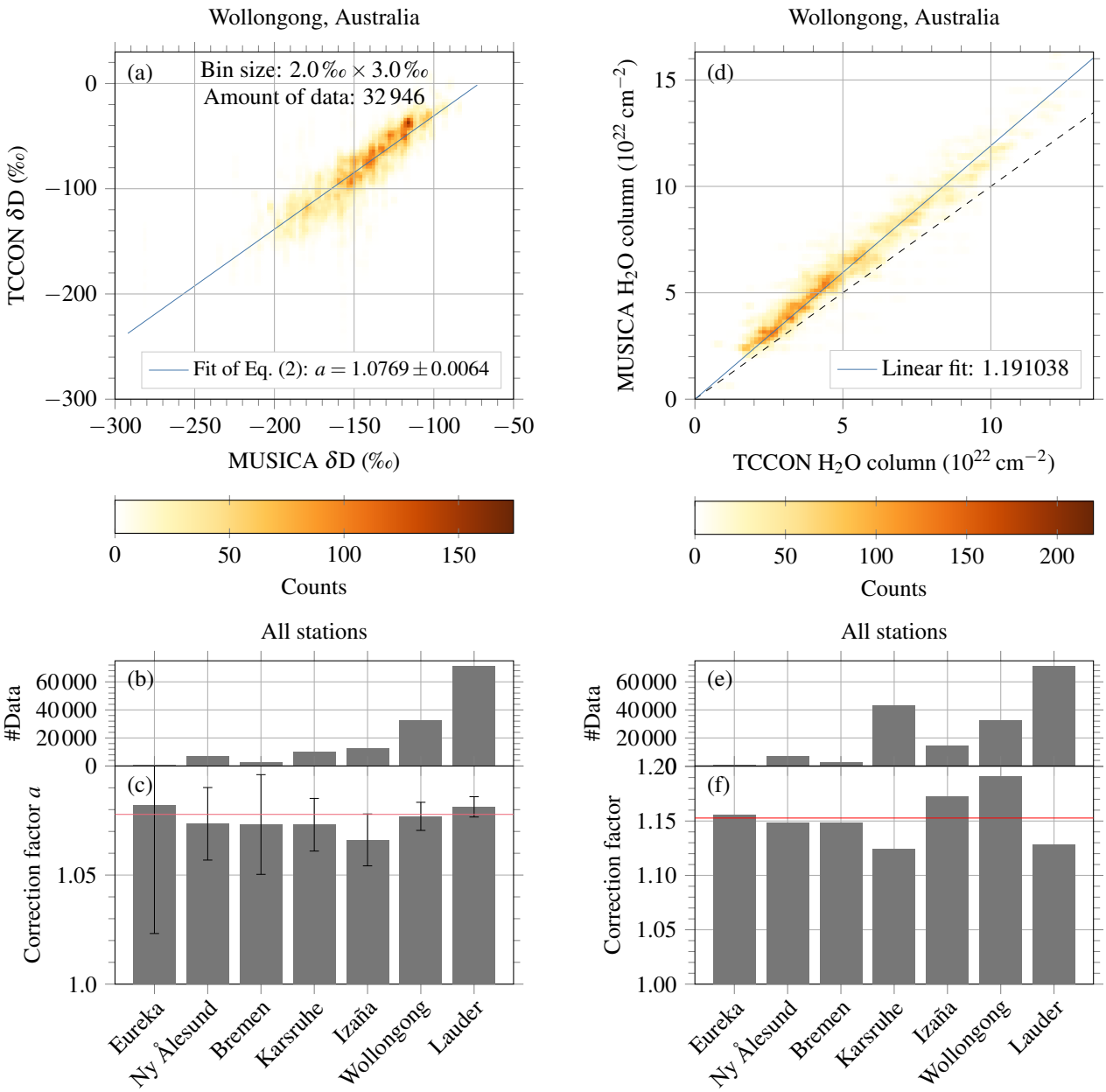

Figure 5: **(a)** Exemplary correlation histogram of TCCON δD vs. MUSICA δD for Wollongong, Australia. The blue line shows the result of a fit of Eq. (3), giving the correction factor for TCCON HDO. **(b)** Amount of collocated measurements for all stations in both networks. **(c)** Fit results of correction factors for individual stations. The red line corresponds to the error-weighted average over all stations, $a = 1.0778$. **(d)** Histogram of collocated TCCON and MUSICA H_2O columns at Wollongong (colour-coded) and result of a fit of a linear correction (blue line). **(e)** Number of collocated observations for all individual stations in both networks. **(f)** Correction factors to correct MUSICA H_2O columns to TCCON. The average 1.1527 is marked by a red line.

Thus it is meaningful to scale HDO at all TCCON stations by the error-weighted average correction factor $a = 1.0778$ in order to correct TCCON's bias in HDO and thus a posteriori δD.

On the other hand, MUSICA-NDACC H_2O is validated only in a limited altitude range of 2–7 km, while TCCON H_2O is much better validated with radiosonde profiles from the ground to ~30 km height. Thus, TCCON H_2O is considered more reliable than MUSICA-NDACC H_2O. Figure 5d shows a correlation plot of H_2O columns at Wollongong, Australia. The difference is well described by a simple scaling of the column. The result of such a fit for all stations in both networks, including recent data that has become available in 2020, is presented in Fig. 5f. The correction factors do not vary considerably between stations. To harmonise both data sets, MUSICA H_2O and HDO columns are thus corrected by dividing by the mean correction factor 1.1525 (red line in Fig. 5f). This adjusts the MUSICA H_2O columns while leaving δD unchanged.

3.2.4 Collocation

To collocate ground and satellite observations, the usual approach is to select satellite ground pixels within a circle around the ground station with given maximal time lag to a ground measurement. An FTIR instrument has a directional sensitivity in its viewing direction, and if the sun is low in the sky (i. e. for high solar zenith angles), this translates into an azimuthal sensitivity, while there is no azimuthal dependency if the sun is in the zenith. To take this into account, the collocation here considers satellite overpasses in a cone in FTIR viewing direction with an opening angle α and a radius r_α depending on solar zenith angle φ. Varying the opening angle linearly with SZA from α_0 at $\varphi = 90°$ to 360°at $\varphi = 0°$ and requiring equal collocation area in all cases gives

$$\alpha(\varphi) = \alpha_{90} + \frac{90° - \varphi}{90°}(360° - \alpha_{90}) \tag{4}$$

$$r_\alpha = \sqrt{\frac{360°}{\alpha}}\, r_0. \tag{5}$$

Figure 6 illustrates this condition, which selects ground pixels depending on the directional sensitivity of the FTIR while keeping the collocation area constant. Here, $\alpha_{90} = 45°$ and $r_0 = 10.6$ km, which corresponds to $r_{90°} = 30$ km.

The time between satellite and ground measurements has to be less than 2 h to minimise representation errors due to the diurnal cycle. Only TROPOMI ground pixels with an altitude difference to the station height of less than 500 m are taken into account. If the altitude difference is too large, the observation of different partial columns leads to errors.

The effects by different a priori profiles used by FTIR and satellite retrievals are corrected for with the column averaging kernel. Following Borsdorff et al. [2014], the column c_i retrieved using prior profile $\mathbf{x}_{\mathrm{a}i}$ can be corrected for using prior profile $\mathbf{x}_{\mathrm{a}j}$ with the column averaging kernel $\mathbf{A}_i$ of retrieval i by

$$c_\mathrm{s} = c_i + (\mathbf{1} - \mathbf{A}_i)^T \mathbf{x}_{\mathrm{a}j} \tag{6}$$

where $\mathbf{1}$ is a vector of ones. The letter "s" stands for smoothed. In the present case, i is TROPOMI and j is TCCON. TCCON prior profiles are linearly interpolated from TCCON levels to SICOR layer centres, and the top layer is extended to 0 Pa. This correction is performed for all comparisons except for high-altitude stations.

3.2.5 Scattering cross-sections

Experiments with different cross-section tables have been performed to determine their effect on the retrieval. To this end, a run for the whole world for three days starting at 20th September 2018 was performed, where cross-sections for H_2O,

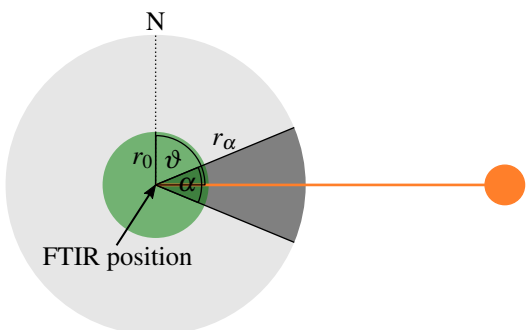

Figure 6: Illustration of the spatial collocation condition. The collocation area consists of a cone in FTIR viewing direction (i. e. solar azimuth angle ϑ) with opening angle α and radius r_α depending on solar zenith angle φ (dark grey). The limit of $\varphi = 0°$ is a full circle (green). The area remains constant (dark grey and green).

HDO and CH_4 have individually been exchanged, and an additional run with all cross-sections (H_2O, HDO, $H_2{}^{18}O$, CH_4, CO) exchanged. First, before the beginning of the fellowship, HITRAN 2008 with extensions by Scheepmaker et al. [2013] as described in the proposal has been compared to the new release HITRAN 2016. Later, HITRAN 2016 cross-sections have been compared to those by the Scientific Exploitation of Operational Missions (SEOM) Improved Atmospheric Spectroscopy Databases (IAS) project. Corresponding results are shown in 3.4.1.

3.2.6 Effective cloud parameter retrieval with ERS

As described above in Sec. 3.2.1, elevated reflecting surface (ERS) is a simple cloud model assuming a partial coverage (determined by cloud fraction f) with a non-transparent thin layer with cloud albedo a and cloud height h. Due to interferences, it is not possible to fit both surface albedo and cloud albedo. Thus, an effective cloud albedo is determined by runs with different fixed values over the ocean (where surface albedo is known to be zero, as water is very dark in the SWIR). In these runs, the surface albedo has been set to zero to minimise cross-dependencies. The best effective cloud albedo is determined by comparing the inferred cloud fraction and cloud height to the VIIRS EDR data product. The result is that at a cloud albedo of 0.1 the agreement between retrieved cloud parameters and VIIRS is best.

A comparison of runs with prescribed surface albedo and free fitted surface albedo shows that interferences between cloud parameters and surface albedo have been present. This is particularly visible over oceans, where the real surface albedo is known to be zero. There are even unphysical values of surface albedos above 1 present. Apparently, clouds are misinterpreted as surface albedo. To eliminate these artefacts, it has been decided to provide a prior on surface albedo based on the average albedo of the non-scattering retrieval (or zero over oceans), and to regularise the surface albedo. This has first been tested for TCCON stations where the average of all collocated clear-sky non-scattering retrievals has been used as prior.

The regularisation has been optimised for scenes over oceans where the real ground albedo is well known (it is 0). The misinterpretations can be largely reduced. Thus, it has been decided to create an albedo map based on one year averages of the non-scattering retrieval to be used as prior for the scattering retrieval. Figure 7 plots the result.

With the new parameters, a TCCON validation has been performed. For filtering, the sensitivity near ground in terms of the averaging kernel has been used. Scenes where the averaging kernel in the lowest layer deviates from 1 by more than 0.3 are discarded. This effectively selects clear-sky scenes. The regularisation of the surface albedo also improves the validation. However, at most stations the bias in the water vapour columns is still much larger than for the non-scattering retrieval. Furthermore, the amount of non-convergences is high. Potentially, clouds are not so uniform that they can be described with fixed cloud albedo. Thus, it has been decided not to use the ERS model.

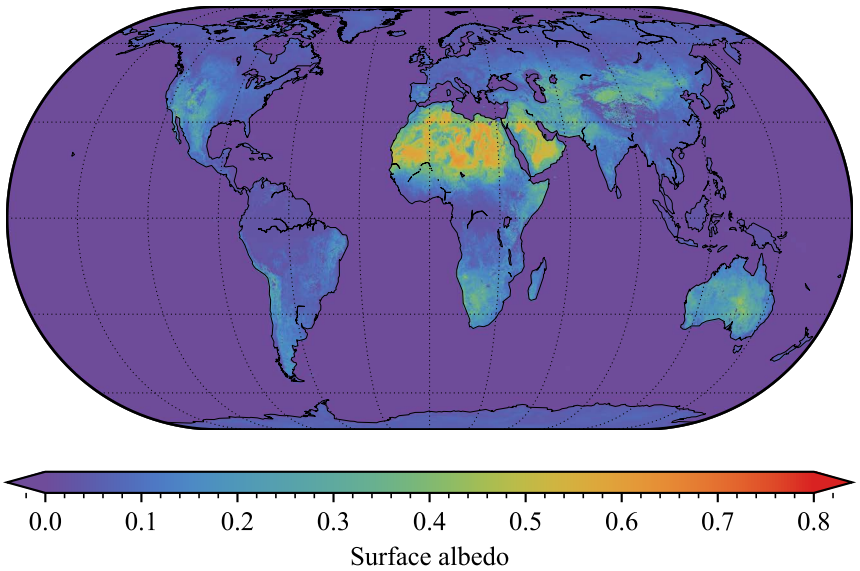

Figure 7: Surface albedos from the non-scattering retrieval averaged over the year 2018. Values over oceans and lakes (where the non-scattering retrieval does not yield data) are set to 0.

3.2.7 Effective cloud parameter retrieval with PIFM

For the PIFM two-stream radiative transfer model, SICOR implements a cloud model that assumes a single scattering layer with a triangular height profile in extinction coefficient centred at cloud centre height h with a geometrical half-width d and a cloud optical thickness of τ. The first approach is to fit the effective cloud parameters simultaneous to the trace gases analogous as done for the CO product [Landgraf et al., 2016]. The cloud geometric thickness d is fixed because fitting both d and τ would lead to ambiguities. Experiments with different geometric thicknesses over the ocean and at TCCON stations have been performed to determine the best value. Generally, the dependence on the geometric thickness is small. Thinner clouds slightly improve the validation but also result in significantly less convergences. Finally, the value of $d = 2500$ m used by Scheepmaker et al. [2016] is kept.

Since interferences between surface albedo and cloud optical thickness are expected, surface albedos are regularised to the one-year average of the non-scattering retrieval similarly as with the ERS model. The regularisation strength has been optimised with retrievals over the ocean and at TCCON stations. This reduces unrealistic surface albedo values similarly as with the ERS model.

PIFM also has the fixed internal parameters Ångström parameter, single scattering albedo (ssa) and asymmetry parameter. These are optimised by varying each parameter individually and looking at the effect on surface albedo, cloud parameters and their comparison to VIIRS, as well as trace gasses. Varying the Ångström parameter changes very little. Increasing the asymmetry parameter leads to less convergences and more extreme surface albedos, so it is kept at its original value. Increasing the ssa reduces misinterpretations between surface albedo and cloud optical thickness while changing water vapour columns as well. Finally ssa is increased to 0.97 with surface albedo regularisation weight 100.

With these optimised parameters, the retrieved water vapour columns still have high biases, and the differences between retrieved effective cloud parameters and VIIRS are large. Since the cloud parameters are estimated from the difference in retrieved methane to the prior, different methane priors are tried. However, using CAMS instead of TM5 changes very little.

After many experiments with different setups, it has been noted by extending the TCCON validation to the methane columns that the non-scattering retrieval (which produces good results for H_2O/HDO) has a large bias in the (side-) retrieved methane compared to TCCON. The spectral range is not optimal to retrieve CH_4, thus methane is an effective parameter and can deviate from the truth. This hints that fitting h and τ in the same spectral range as the trace gases seems not to work, maybe due to interferences and/or inaccuracies of the methane spectroscopy. To overcome this problem, it has been decided to fit cloud parameters in a pre-fit in another spectral window and take over the result to the final retrieval in the HDO window, fixing cloud parameters and fitting methane instead. This neglects the spectral dependence of the cloud optical thickness. Nine different spectral windows in the range 2310 nm to 2385 nm have been tested with different a priori values for cloud height (2000 m, 1500 m, 1000 m, 0 m), cloud optical thickness (1.0, 0.5, 0.2, 0.0) and cloud geometric thickness (2500 m, 1000 m), and different regularisation of the cloud height (5, 3, 0). Runs have been performed over the ocean and at the TCCON station Edwards. After evaluation of the number of convergences, differences between inferred effective cloud parameters and VIIRS EDR, the classification of clear-sky scenes of the retrieval and VIIRS, and the bias in retrieved H_2O/HDO columns to TCCON, the window 2310 nm – 2338 nm has been selected as it performs best. As visualised in Fig. 8, large absorption features of methane not interfering with H_2O are present in this window.

Filter criteria have been optimised by looking at the dependence of the bias against TCCON on various quantities (such as solar zenith angle, viewing zenith angle, χ^2, root mean square of the residual, surface albedo, cloud height, cloud optical thickness). Table 4 summarises the final choices. Retrievals are filtered for convergence and with a quality filter based on fit quality in terms of the number of iterations and χ^2 as measure for the residual. Moreover, scenes with

Table 4: Quality filters and selection criteria for clear-sky and cloudy-sky conditions.

Quantity	Filter
Quality filter (all scenes)	
Number of iterations	$n \leq 10$
Reduced χ^2	$\chi^2_{\mathrm{f}} \leq 150$
Reduced χ^2 of pre-fit	$\chi^2_{\mathrm{p}} \leq 150$
Solar zenith angle	$\varphi \leq 70°$
Clear-sky filter	
Cloud optical thickness	$\tau_{\mathrm{cld}} < 0.3$
Surface albedo	$a \geq 0.02$
Filter for cloudy scenes	
Cloud height	$h_{\mathrm{cld}} \leq 2000$ m
Cloud optical thickness	$\tau_{\mathrm{cld}} > 0.3$

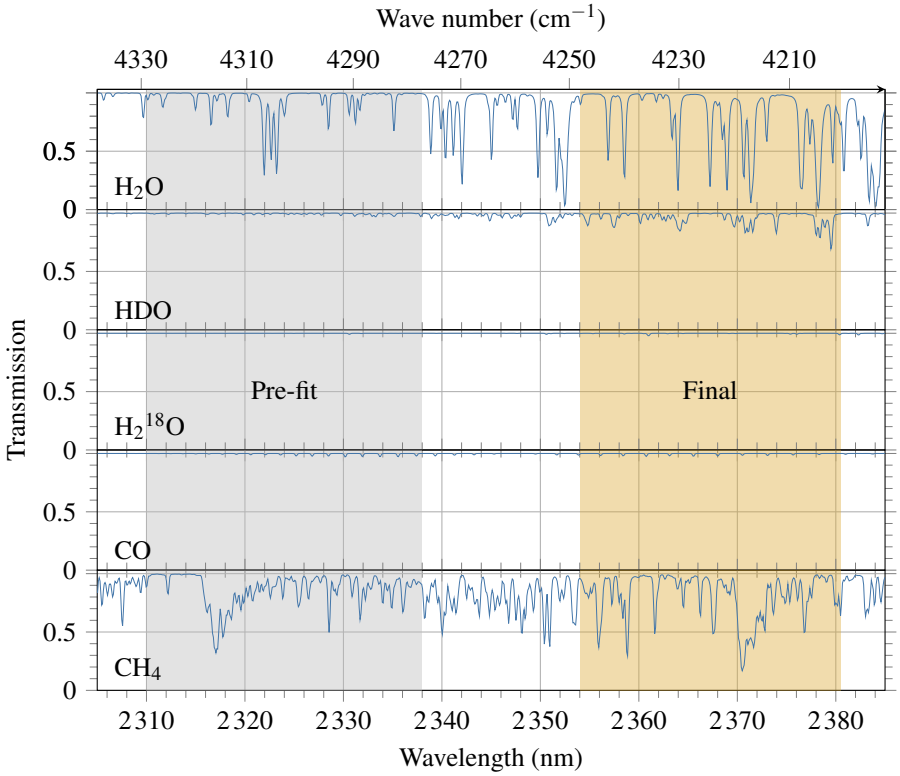

Figure 8: Simulation of atmospheric transmission in the spectral range of TROPOMI's SWIR channel for the absorbers taken into account by the retrieval algorithm. The grey shading marks the spectral window used for the determination of effective cloud parameters, the yellow shading the spectral window for the retrieval of the trace gases.

high solar zenith angles are filtered out since they are prone to errors due to multi-scattering and diffraction effects not covered well by the forward model and due to typically low radiances resulting in low signal-to-noise ratios. From the remaining data, scenes are classified as clear-sky, cloudy with low clouds, or other (e. g. high clouds) based on retrieved effective cloud parameters as specified in Tab. 4. Only scenes of the first two categories (i. e. clear-sky or low clouds) are considered in this study and recommended to be taken into account by the user, except if the data are assimilated using averaging kernels. Clear-sky scenes are additionally filtered for surface albedo because low surface albedos usually involve low signal-to-noise ratios. Such a surface albedo filter is not applied to cloudy scenes because clouds usually have high reflectivity and shield the surface, which allows to retrieve over very low surface albedos with high signal-to-noise ratio.

3.2.8 Retrieving $H_2{}^{18}O$

The proven non-scattering retrieval has been extended to additionally fit $H_2{}^{18}O$. Hardly any reference data are available for validation. The ISOWAT instrument on IAGOS-CARIBIC has technical problems and thus produces no data [A. Zahn, private communication]. Recent NDACC-MUSICA data have become available for three stations in 2020, one of which is a high-altitude station not suitable for validation. This leaves only two sites with reference data including the isotopologue $H_2{}^{18}O$ during the time of the TROPOMI mission, namely Karlsruhe and Kiruna. Runs at these two sites have been performed. Figure 9 shows the retrieval results vs. the reference measurements at Karlsruhe, the station with best results. The retrieved $H_2{}^{18}O$ and especially $\delta^{18}O$ are far off. There is practically no correlation between retrieved $\delta^{18}O$ and the reference $\delta^{18}O$ (Person correlation -0.17). For a usable product, correct $\delta^{18}O$ values are essential. The conclusion is that the signal is too weak to fit $H_2{}^{18}O$ with the required precision.

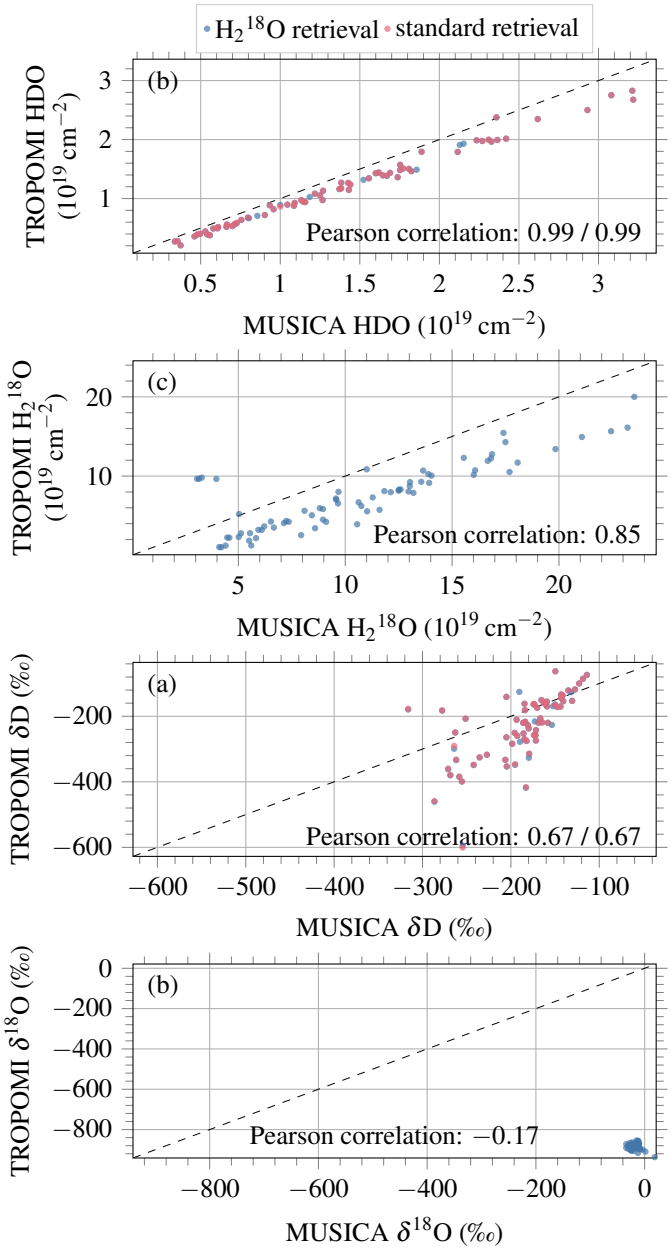

Figure 9: Correlation plots TROPOMI vs. MUSICA at Karlsruhe

3.3 Data

3.3.1 Input data to the retrieval

- TROPOMI L1b radiance data band 7 and 8, available at `https://s5phub.copernicus.eu`
- TROPOMI L1b irradiance data, available at `https://s5phub.copernicus.eu`
- pressure, temperature, and water vapour profiles from ECMWF analysis product
- CH4 and CO profiles from TM5 model output [Krol et al., 2005]
- digital elevation model `http://viewfinderpanoramas.org/dem3.html`
- scattering cross-sections of H_2O, HDO, $H_2{}^{18}O$, CH_4 and CO
  - HITRAN 2008 [Rothman et al., 2009] with updates by Scheepmaker et al. [2013]
  - HITRAN 2016 [Gordon et al., 2017], available at `www.hitran.org`
  - SEOM-IAS, DOI `https://dx.doi.org/10.5281/zenodo.1009126`
- TROPOMI instrument spectral response function (ISRF) [van Hees et al., 2018]
- solar reference spectrum [Ludewig et al., 2020, Sec. 13]

3.3.2 Validation data

- ground-based TCCON data as specified in Tab. 3, 6, 7, and 8, available from `https://tccondata.org/`
- ground-based MUSICA-NDACC data as specified in Tab. 3, available from `ftp://ftp.cpc.ncep.noaa.gov/ndacc/MUSICA/`
- aircraft-based WISPER data, available from `https://espoarchive.nasa.gov/archive/browse/oracles/P3/mrg1`

3.4 Results

3.4.1 Influence of scattering cross-sections

Before the beginning of the fellowship, a comparison between the HITRAN 2008 cross-sections with updates by [Scheepmaker et al., 2013] (as mentioned in the proposal) and the new HITRAN 2016 release has been performed. Results in Figs. 10 and 11 show that both the fit quality in terms of χ^2 and the validation improve drastically with the updated cross-sections. Thus, HITRAN 2016 is used.

Later, the effect of changing scattering cross-sections from HITRAN 2016 to those by the Scientific Exploitation of Operational Missions (SEOM) Improved Atmospheric Spectroscopy Databases (IAS) project has been studied. To this end, a run of the non-scattering retrieval for the whole world for three days starting at 20th September 2018 has been performed, where cross-sections for H_2O, HDO and CH_4 have individually been exchanged, and an additional run with all cross-sections (H_2O, HDO, $H_2{}^{18}O$, CH_4, CO) exchanged. Figure 12 depicts the change in fit quality in terms of χ^2.

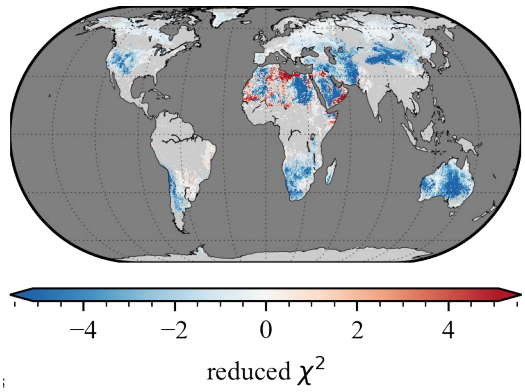

Figure 10: Relative difference in χ^2 when replacing HITRAN 2008 cross-sections with updates by Scheepmaker et al. [2013] by HITRAN 2016 cross-sections

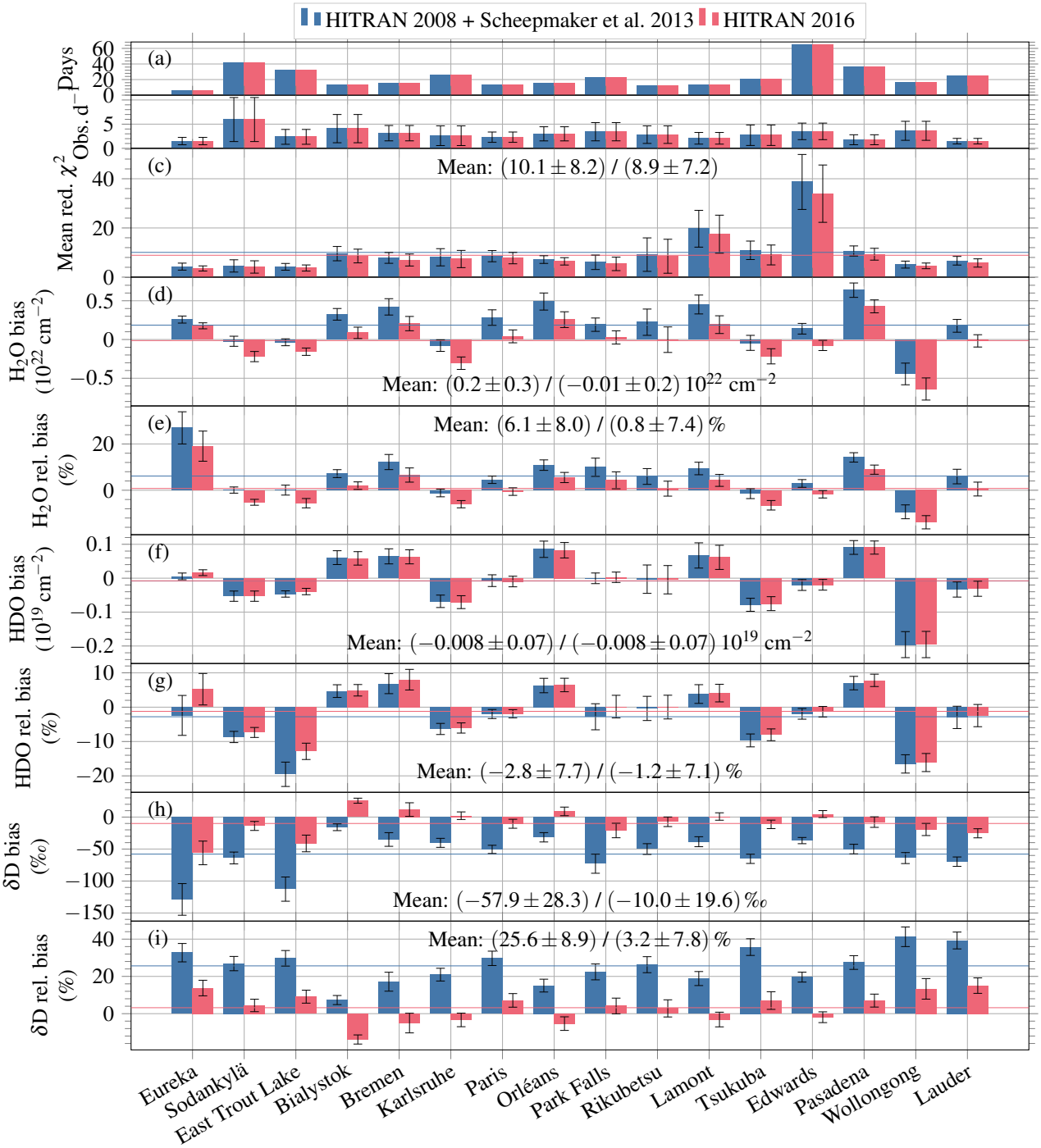

Figure 11: Validation for retrievals with HITRAN 2008 cross-sections with updates by Scheepmaker et al. [2013] (blue) and HITRAN 2016 cross-sections (red)

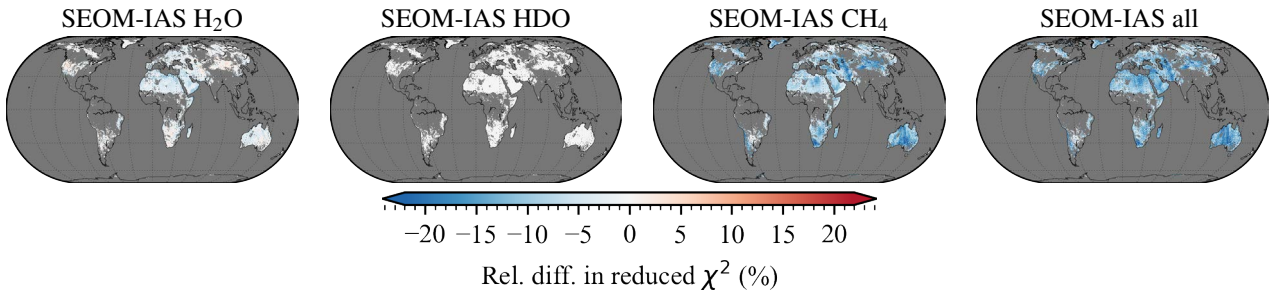

Figure 12: Relative difference in χ^2 when replacing HITRAN 2016 cross-sections by those from SEOM-IAS.

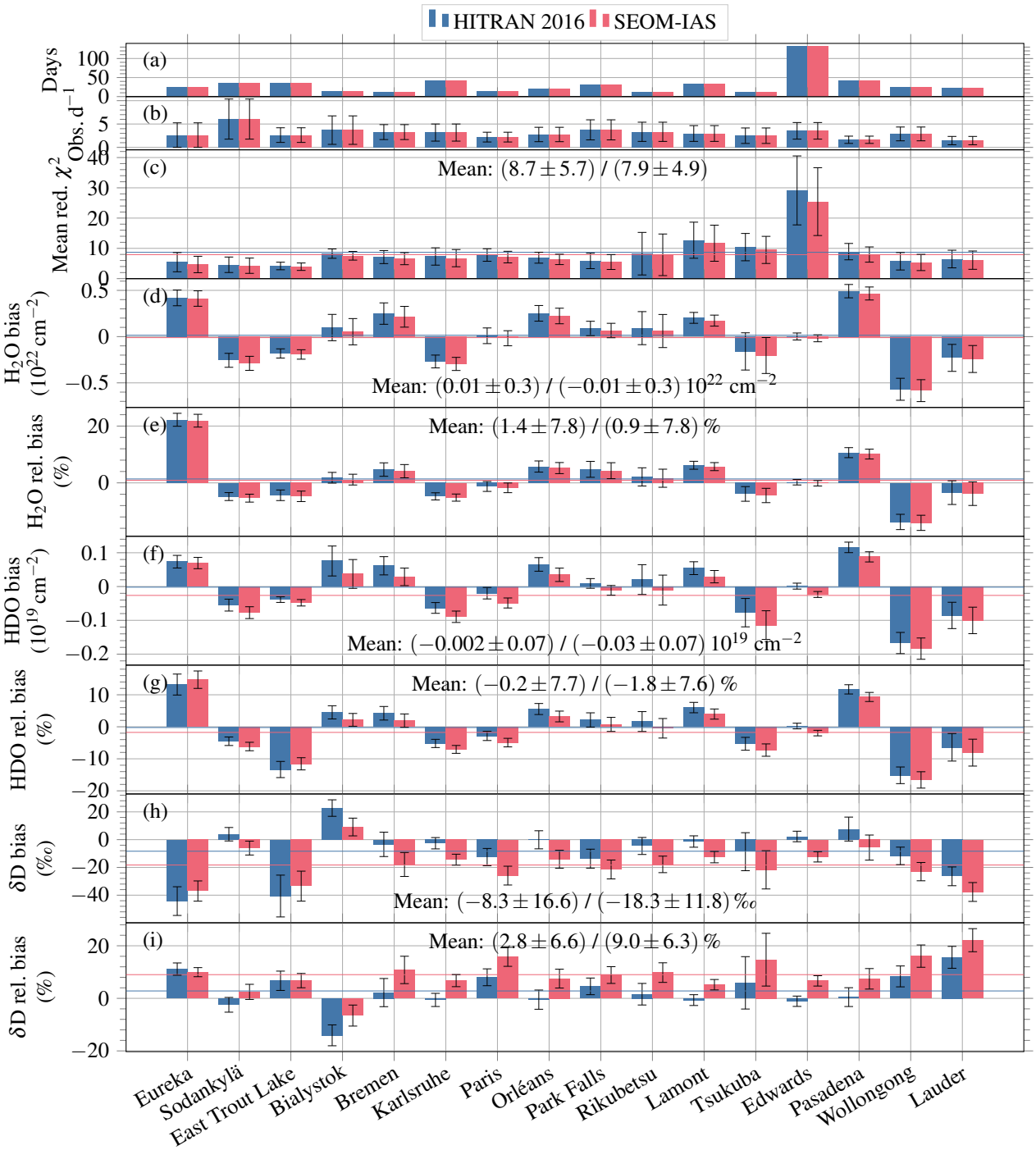

Figure 13: Validation for retrievals with HITRAN 2016 cross-sections (blue) and cross-sections from the SEOM-IAS project (red)

Especially the updated cross-sections of methane yield a significant improvement in fit quality, while those of H_2O and HDO do not change χ^2 much. Furthermore, runs for groundpixels collocated with TCCON stations have been performed for the whole time series. Figure 13 shows the validation results. Averaging kernels have been accounted for as described in Sec. 3.2.4. The SEOM-IAS cross-sections yield a slight improvement in the bias of H_2O from 1.4 % to 0.9 %, but the bias in HDO is worse with an increase from −0.2 % to −1.8 %, which results in a huge worsening of the bias in a posteriori δD from −8 ‰ to −18 ‰. Table 5 summarises the results for the individual runs. The increased bias is more important than the improvement in fit quality. Thus, the conclusion is to stick with HITRAN 2016. As a side remark, some lines from the SEOM-IAS project have already been taken over by HITRAN 2016.

Table 5: Averaged χ^2 for three days in September 2018 and bias in δD for the whole time series in dependence of different selections of cross-sections.

Description	χ^2	Bias δD
HITRAN 2016	36.6	−8 ‰
SEOM-IAS	34.2	−18 ‰
H_2O SEOM-IAS, rest HITRAN 2016	37.0	−30 ‰
HDO SEOM-IAS, rest HITRAN 2016	38.4	−12 ‰
CH_4 SEOM-IAS, rest HITRAN 2016	35.3	+8 ‰

3.4.2 Validation of the non-scattering retrieval

Table 6 lists the stations that are used for the validation. For each station, daily averages are computed over all collocated measurements. Figure 14 shows an exemplary time series for Edwards station. The collocated observations of H_2O and HDO agree very well, and the agreement in δD is also good, with more scatter and a small bias. Corresponding correlation plots are depicted in Fig. 15. Figure 15a and b confirm the excellent agreement in H_2O and HDO with Pearson correlation coefficients of 0.99. A posteriori δD has a correlation coefficient of 0.73.

Figure 16 depicts the validation statistics for all TCCON stations. The correlation in H_2O and HDO is high for all stations. In δD, the correlation is high except for a low correlation of 0.37 at JPL. The average difference between TROPOMI and TCCON defines the bias. Figure 17 shows biases at all stations. At low- and mid-latitude ($< 54°$) stations the bias is as low as $(-0.1 \pm 1) \times 10^{21}$ molec cm^{-2} (corresponding to a relative bias of (-0.5 ± 2.8) %) in H_2O and $(-0.6 \pm 3) \times 10^{17}$ molec cm^{-2} ((-1.0 ± 3.0) %) in HDO, which corresponds to (-6 ± 12) ‰ (3.2 ± 6.5 %) in a posteriori δD. At these stations the bias in δD ranges between about -25 ‰ and $+25$ ‰. At high-latitude stations it can be as high as -40 ‰ to -55 ‰. Possible reasons for these high biases are higher relative biases in H_2O and/or HDO at

Table 6: List of ground stations used for the validation of the non-scattering retrieval.

Station	Latitude	Longitude	Altitude	Data available from/to	Reference
Eureka	80.1° N	86.4° W	610 m	24 Jul 2010 – 07 Jul 2020	Strong et al. [2019]
Sodankylä	67.4° N	26.6° E	190 m	16 May 2009 – 30 Oct 2019	Kivi et al. [2014]
East Trout Lake	54.4° N	105.0° W	500 m	07 Oct 2016 – 04 Jul 2020	Wunch et al. [2018]
Bialystok	53.2° N	23.0° E	190 m	01 Mar 2009 – 01 Oct 2018	Deutscher et al. [2019]
Bremen	53.1° N	8.9° E	30 m	15 Jan 2007 – 23 Aug 2019	Notholt et al. [2019a]
Karlsruhe	49.1° N	8.4° E	110 m	19 Apr 2010 – 31 Jul 2020	Hase et al. [2015]
Paris	48.8° N	2.4° E	60 m	23 Sep 2014 – 23 Jul 2019	Té et al. [2014]
Orléans	48.0° N	2.1° E	130 m	29 Aug 2009 – 31 Jul 2019	Warneke et al. [2019]
Park Falls	45.9° N	90.3° W	440 m	02 Jun 2004 – 02 Apr 2020	Wennberg et al. [2017]
Rikubetsu	43.5° N	143.8° E	380 m	16 Nov 2013 – 31 Jul 2019	Morino et al. [2018c]
Lamont	36.6° N	97.5° W	320 m	06 Jul 2008 – 01 Apr 2020	Wennberg et al. [2016b]
Tsukuba	36.0° N	140.1° E	30 m	04 Aug 2011 – 31 Jul 2019	Morino et al. [2018a]
Edwards	35.0° N	117.9° W	700 m	20 Jul 2013 – 04 Jul 2020	Iraci et al. [2016]
JPL	34.2° N	118.2° W	390 m	19 May 2011 – 14 May 2018	Wennberg et al. [2016a]
Pasadena	34.1° N	118.1° W	240 m	20 Sep 2012 – 03 Jul 2020	Wennberg et al. [2015]
Saga	33.2° N	130.3° E	10 m	28 Jul 2011 – 04 May 2020	Kawakami et al. [2014]
Burgos	18.5° N	120.7° E	40 m	03 Mar 2017 – 22 Aug 2019	Morino et al. [2018b]
Wollongong	34.4° S	150.9° E	30 m	25 Jun 2008 – 31 Jul 2019	Griffith et al. [2014b]
Lauder	45.0° S	169.7° E	370 m	02 Feb 2010 – 04 May 2020	Sherlock et al. [2014], Pollard et al. [2019]

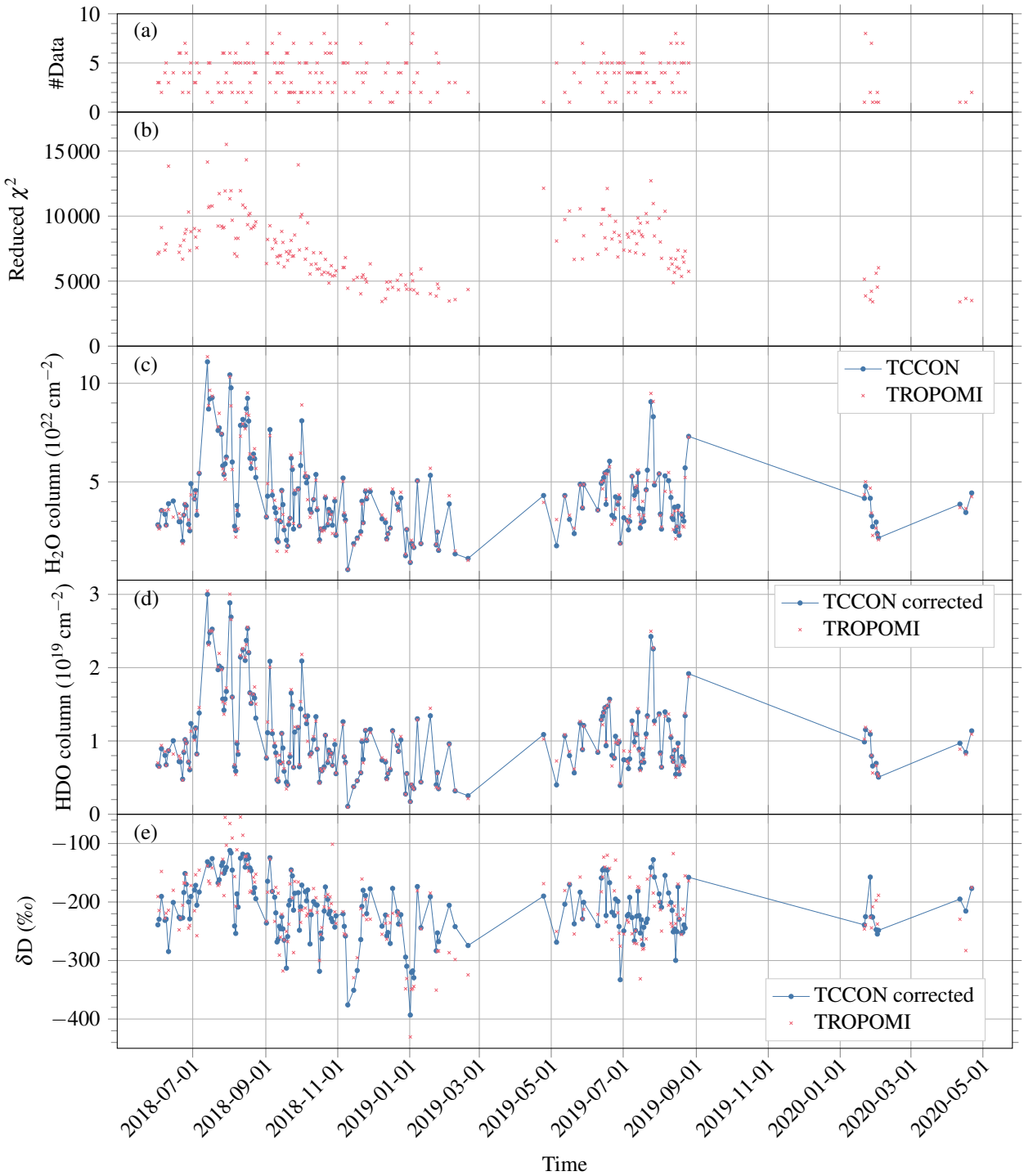

Figure 14: Time series of daily medians of corrected TCCON measurements (blue crosses) and collocated TROPOMI observations (red pluses) at Edwards station (35.0° N, 117.9° W, 700 m a.s.l.). Shown are **(a)** the number of individual observations per day, **(b)** the reduced χ^2, **(c)** the H_2O columns, **(d)** the HDO columns and **(e)** the a posteriori δD.

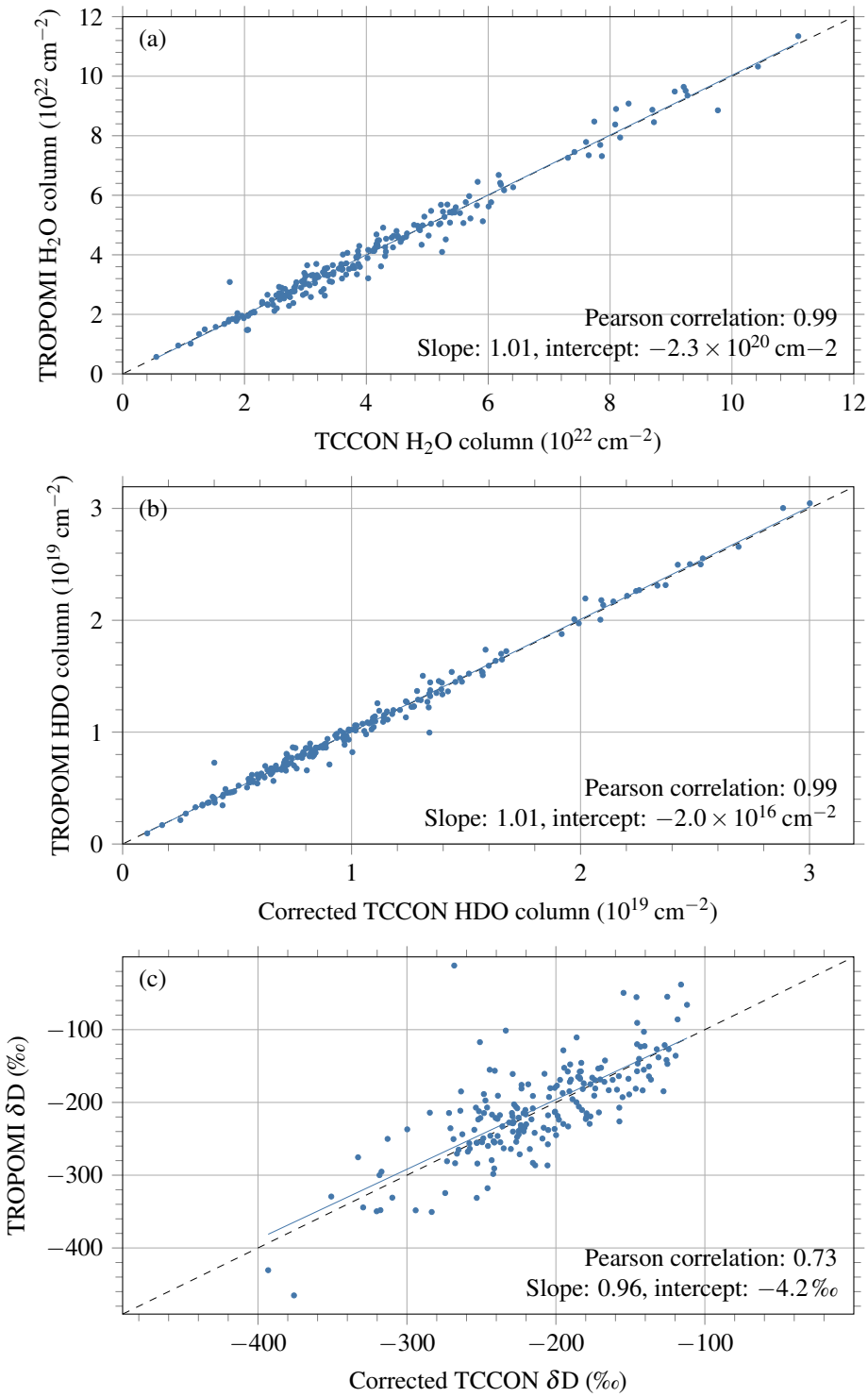

Figure 15: Correlation plot of corrected TCCON measurements and collocated TROPOMI observations for Edwards station for daily averages of H_2O columns **(a)**, HDO columns **(b)** and δD **(c)**. The dashed lines mark equality, and the solid lines give linear fits to the data.

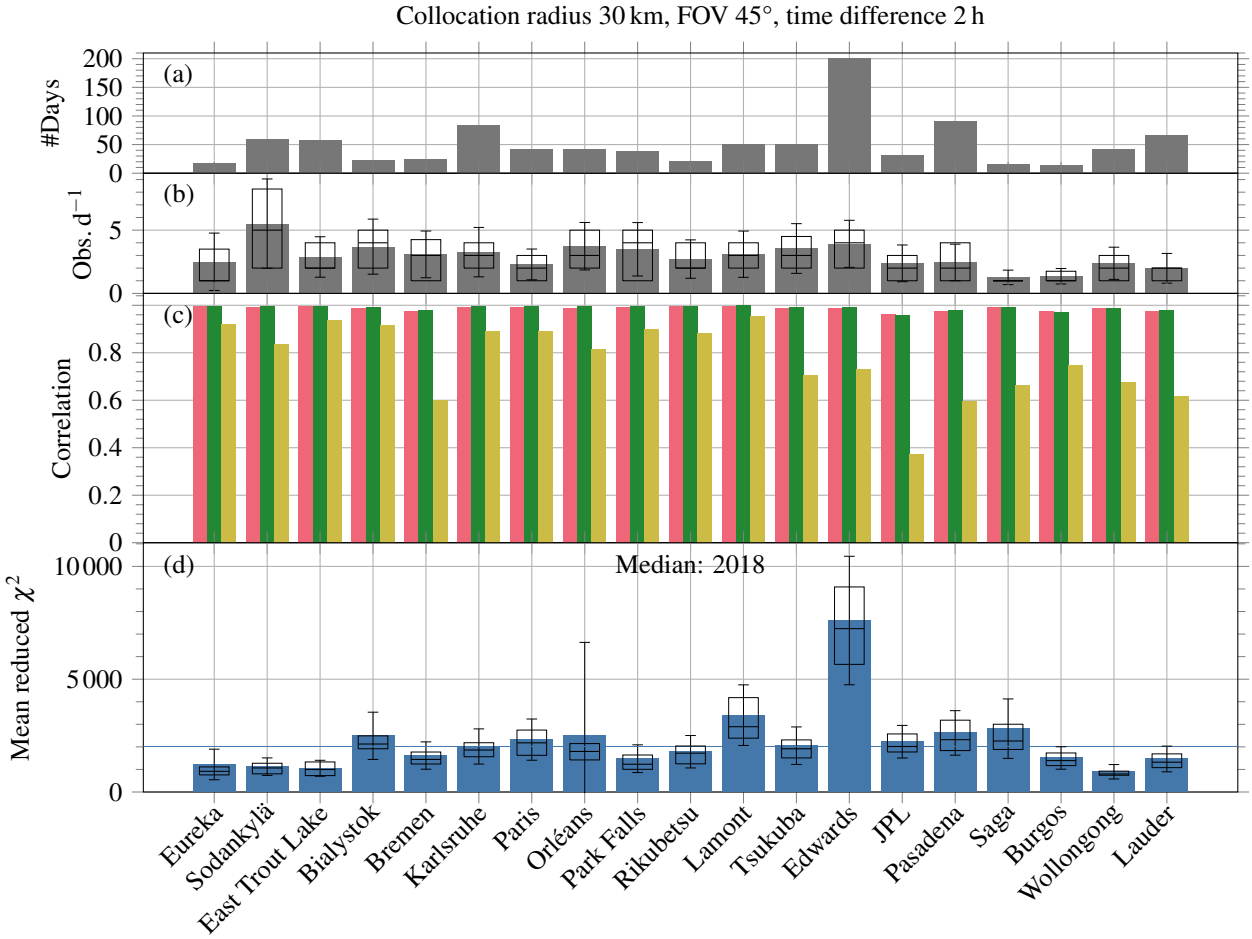

Figure 16: Statistics of the validation for all TCCON stations. **(a)** Number of days with collocated measurements. **(b)** Average number of collocated TROPOMI observations per day and its standard deviation. **(c)** Pearson correlation coefficient for H_2O (red), HDO (green) and δD (yellow). **(d)** Average reduced χ^2 and its standard error; the blue line visualises the average over all stations.

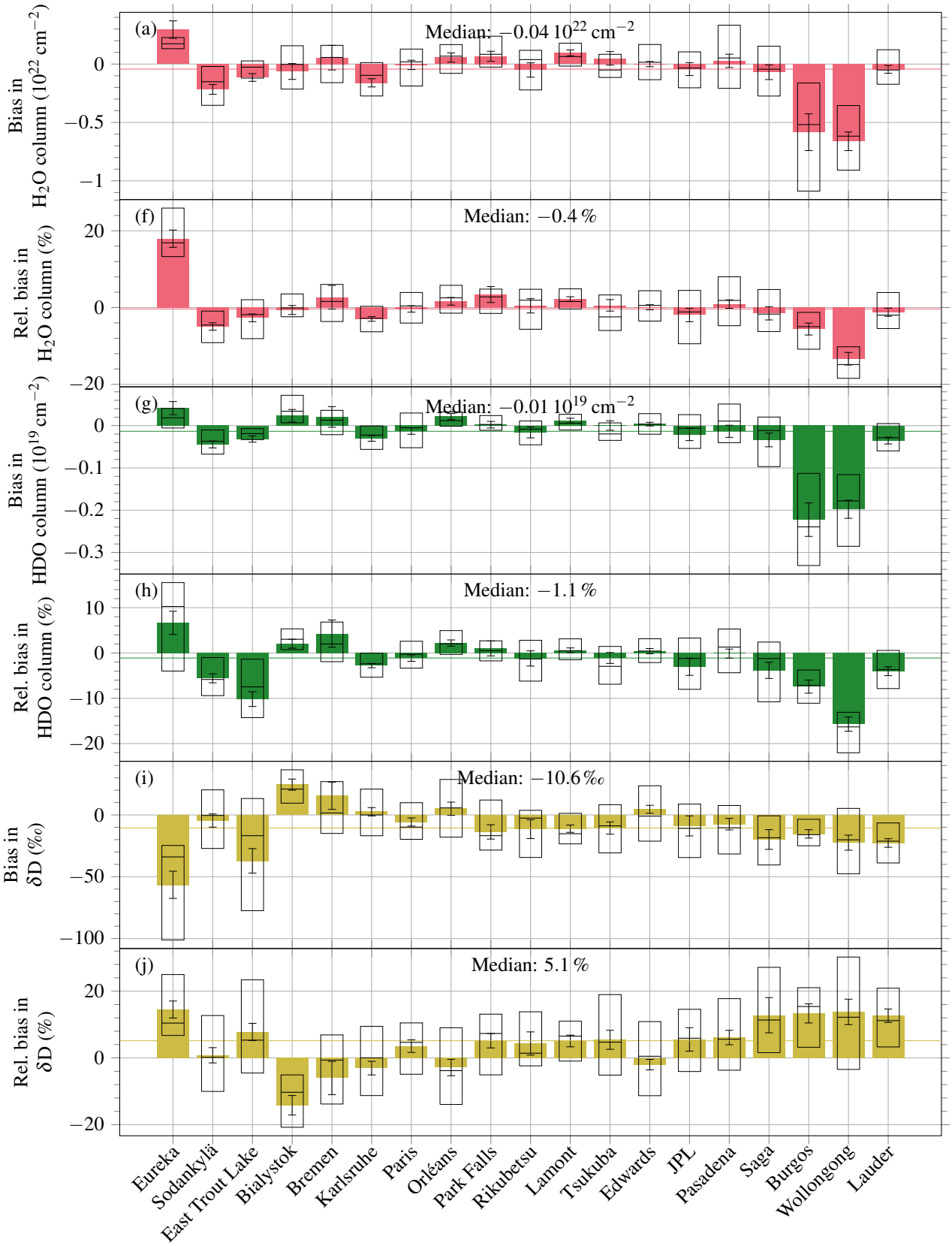

Figure 17: Biases for all TCCON stations with standard error (errorbars) and quartiles (boxes). Shown are **(a)** bias in H_2O, **(b)** relative bias in H_2O, **(c)** bias in HDO, **(d)** relative bias in HDO, **(e)** bias in a posteriori δD, and **(f)** relative bias in a posteriori δD. The horizontal line in all panels visualises the average over all stations.

these relatively dry locations. At high-latitudes, retrievals are generally challenging due to high solar zenith angles and low albedos which lead to low signal-to-noise ratios. The average bias over all stations is $(-0.3 \pm 1) \times 10^{21}$ molec cm^{-2} or (-0.7 ± 3.5) % in H_2O, $(-0.9 \pm 3) \times 10^{17}$ molec cm^{-2} or (-1.3 ± 3.3) % in HDO, and (-7 ± 13) ‰ or (3.8 ± 6.5) % in a posteriori δD. This is good considering that δD is very sensitive to small errors in H_2O or HDO.

3.4.3 Case study using the non-scattering retrieval

An illustration of the TROPOMI retrievals on the global and monthly scale is depicted in Fig. 18 for September 2018. There is no data over the oceans because water is too dark in the short-wave infrared and glint measurements are not taken into account. The data gaps in tropical regions are due to persistent clouds. The data quality in terms of noise is significantly better than for a multi-year average of SCIAMACHY observations, cf. Schneider et al. [2018, Fig. 7]. In the spatial distribution shown in Fig. 18 the major isotopic effects formulated by Dansgaard [1964] can be recognised. The general latitudinal gradient due to the temperature-dependence of the fractionation effects and progressive rain out of heavy isotopologues, the so-called latitudinal effect, is clearly visible. The continental effect of depletion due to rain out of the heavy isotopologue is visible on all continents including Australia. The altitude effect, which describes depletion

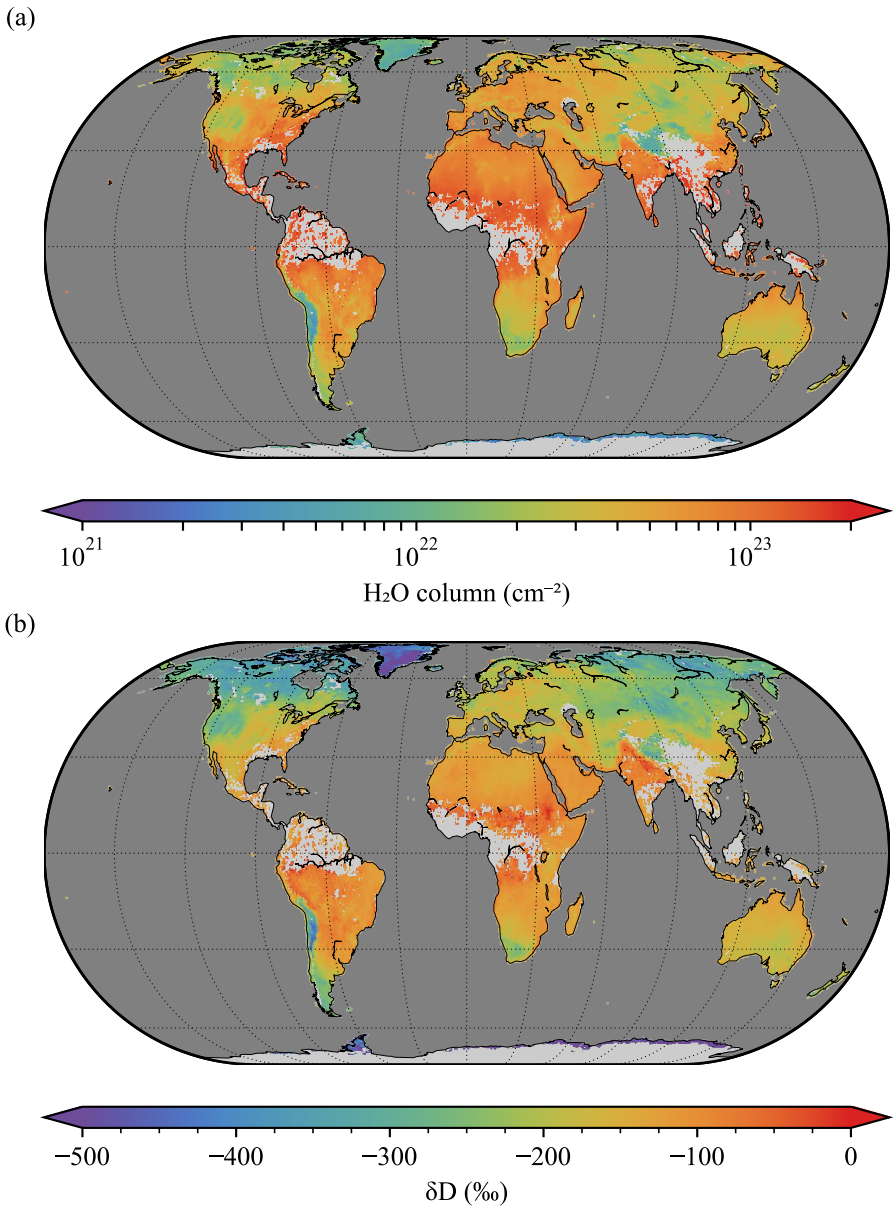

Figure 18: Global plots of H_2O **(a)** and δD **(b)** averaged over September 2018 on a grid of $0.5° \times 0.5°$. The average of δD is weighted with the H_2O column.

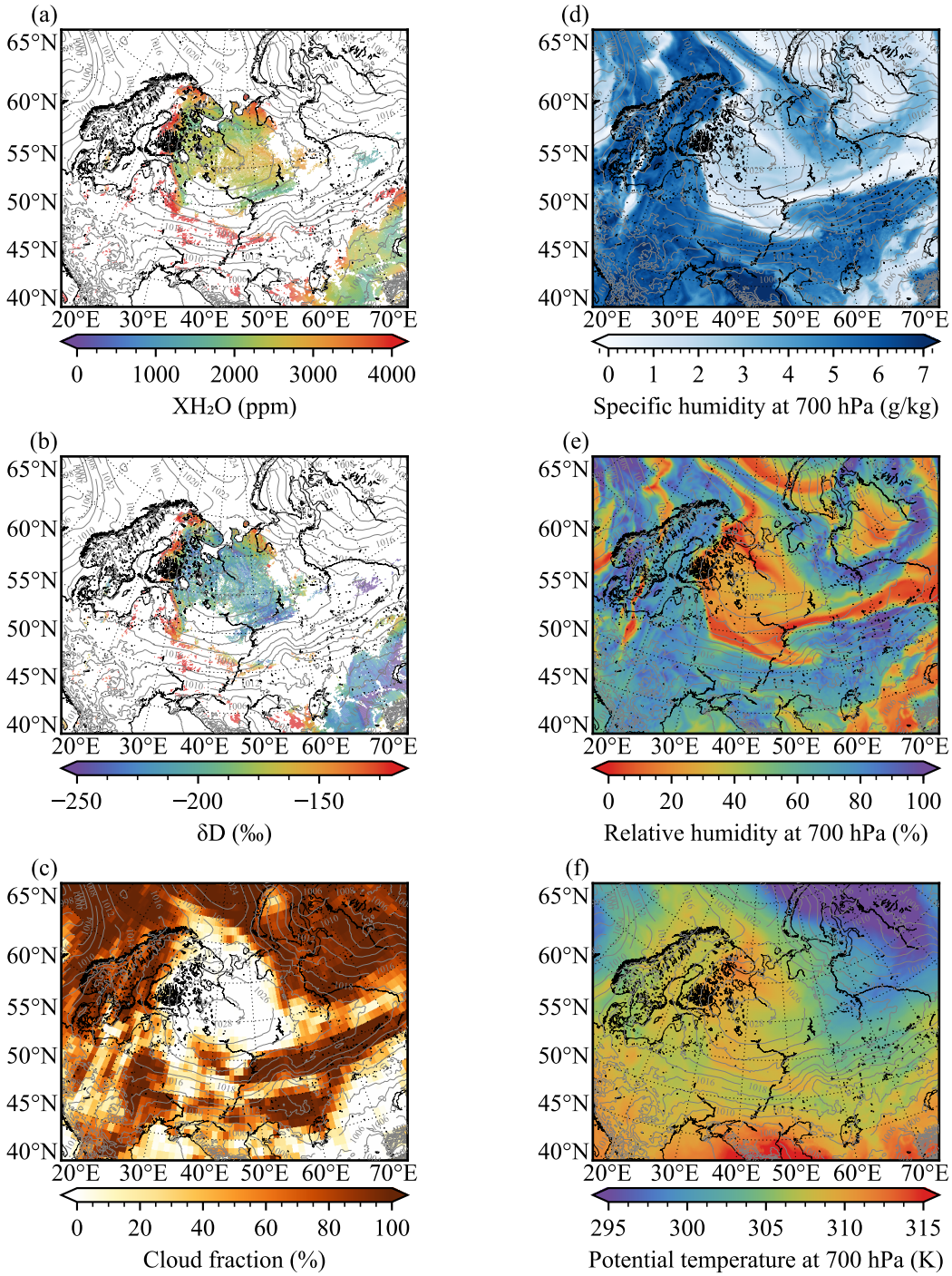

Figure 19: TROPOMI single overpass results for H_2O column **(a)** and δD **(b)** over Europe on 30 Jul 2018; VIIRS cloud fraction on the same day **(c)**; specific humidity **(d)**, relative humidity **(e)**, and potential temperature **(f)** at 700 hPa from the ECMWF analysis product over Europe at 12:00 UTC on 30 Jul 2018. The 700 hPa level is chosen for the thermodynamic variables because it reflects the large-scale conditions in the lower troposphere above the continental boundary layer. The overlaying contours in all panels show mean sea-level pressure from ECMWF at 12:00 UTC with a contour line distance of 2 hPa.

above high ground due to lower temperature and increasing rain out, can be seen, for example, over the Andes and the Himalayas.

To demonstrate the quality and the possibilities of the new data set of water vapour isotopologues from TROPOMI, a case study using single overpass results over Europe on 30th July 2018 is presented in Fig. 19. TROPOMI H_2O and δD are plotted in panels (a) and (b). The regions without data are due to cloud cover (see Figure 19c) or oceans. The synoptic situation shown is a high pressure system over northern Europe that blocked the otherwise predominant westerly moist flow from the North Atlantic and thus caused an exceptionally hot and dry summer in central and northern Europe [Copernicus Climate Service, 2018, Gubler et al., 2018]. Synoptic-scale atmospheric blocking situations can lead to hot temperature extremes due to adiabatic warming of the descending air in the core of the anticyclone [Pfahl and Wernli, 2012]. The descending vertical motion favours clear sky conditions and thus further contributes to the surface warming through radiative effects in the centre of the anticyclone [Trigo et al., 2004]. In particular, the end of July 2018 was characterised by a stationary blocking anticyclone extending over the entire troposphere over northwestern Russia and Scandinavia. This blocking led to large-scale descent and to a divergent flow near the surface in its core, resulting in clear sky conditions over northwestern Russia and Finland (see Fig. 19c). The isotopic signature of the blocking anticyclone in Fig. 19b reflects this synoptic flow configuration with low δD signals of between −250 ‰ and −200 ‰ in the centre of the anticyclone. The depleted total column vapour in this region is due to the large-scale subsidence bringing depleted (Fig. 19b) and dry (Fig. 19d) upper tropospheric air towards lower levels. The near-surface divergent wind exports more enriched freshly evaporated moisture that is taken up near the surface towards the edges of the blocking. The anticyclone area is characterised by clear skies (Fig. 19c) with low specific humidity (1–3 g kg^{-1} at 700 hPa, Fig. 19d), low relative humidity (10–30 % at 700 hPa, Fig. 19e) and high potential temperature associated with the dry subsiding (adiabatically warming) air masses (Fig. 19f). The dry low-level outflow encounters moister and warmer air at the edge of the surface anticyclone, leading to a very strong horizontal gradient of specific and relative humidity (Fig. 19d,e) in the lower troposphere. As a consequence the warm moist air is forced to rise, localised instabilities occur and isolated convective cells develop leading to condensation and the formation of a ring of clouds around the blocking anticyclone. A distinct arc-like feature of enriched total column water vapour at the edge of the anticyclone can be distinguished slightly displaced from the first clouds in the northwest (Fig. 19b). Turbulent mixing and convection injecting more enriched, freshly evaporated moisture advected with the large-scale flow from marine environments (Barents Sea, North Sea and Black Sea) could be the reason for this interesting enriched ring-like water vapour isotopologue pattern. A very depleted cloud free area south of the Ob river with δD values below −250 ‰ (Fig. 19b) might be connected to anomalously strong subsidence of northerly continental air masses.

3.4.4 Validation of the scattering retrieval

Since the scattering retrieval has considerably more coverage, more TCCON stations yield enough data to include in the validation. Table 7 lists the stations used additionally to those in Tab. 6. Collocated cloudy satellite observations require a change in the cloud cover within the collocation radius or the collocation time because the FTIR instrument has to directly see the sun (possibly through gaps in the clouds) to take measurements.

Figure 20 depicts an exemplary time series of daily medians of collocated measurements at the TCCON station Karlsruhe. The TROPOMI observations follow the reference well, although some deviations are present especially for cloudy scenes. Figure 21 presents corresponding correlations. Correlations in the retrieved columns are excellent with a Pearson coefficient of 0.98 in H_2O and 0.99 in HDO for clear-sky scenes, and 0.95 in H_2O and 0.96 in HDO for cloudy scenes. A posteriori δD has slightly more scatter with correlation coefficients of 0.86 and 0.83 for clear-sky and cloudy scenes, respectively. The bias, which is defined as the mean difference between TROPOMI and TCCON, is for clear-sky scenes -1.3×10^{20} cm^{-2} (-0.4 %) in H_2O and -3.6×10^{16} cm^{-2} (-1.0 %) in HDO, which corresponds to a bias in a posteriori δD of -3 ‰ (1.1 %). For cloudy scenes, it is 4.9×10^{21} cm^{-2} (8.3 %) in H_2O, 1.1×10^{18} cm^{-2} (6.5 %) in HDO and -12 ‰ (7.3 %) in a posteriori δD. The retrieval performance for cloudy scenes is good: correlations are similar as for clear-sky scenes or the non-scattering retrieval, although the bias is larger. This can be explained by small sensitivity of the retrieval below optically thick clouds.

Figure 22 presents statistics and correlation coefficients of daily medians at all low-altitude stations. The amount of data for clear-sky scenes of the new scattering retrieval is much larger than for the non-scattering retrieval: on average a factor of 8 more. This is connected to different filtering: while the non-scattering product is strictly filtered with the S5P-VIIRS product and an additional two-band filter (see Tab. 2 in Sec. 3.2.2), the scattering product is filtered with effective

Table 7: List of ground stations used for the validation of the scattering retrieval additionally to those listed in Tab. 6.

Station	Latitude	Longitude	Altitude	Data available from/to	Reference
Ny Ålesund	78.9° N	11.9° E	20 m	28 Mar 2006 – 06 Jul 2019	Notholt et al. [2019b]
Garmisch	47.5° N	11.1° E	750 m	16 Jul 2007 – 18 Oct 2019	Sussmann and Rettinger [2018a]

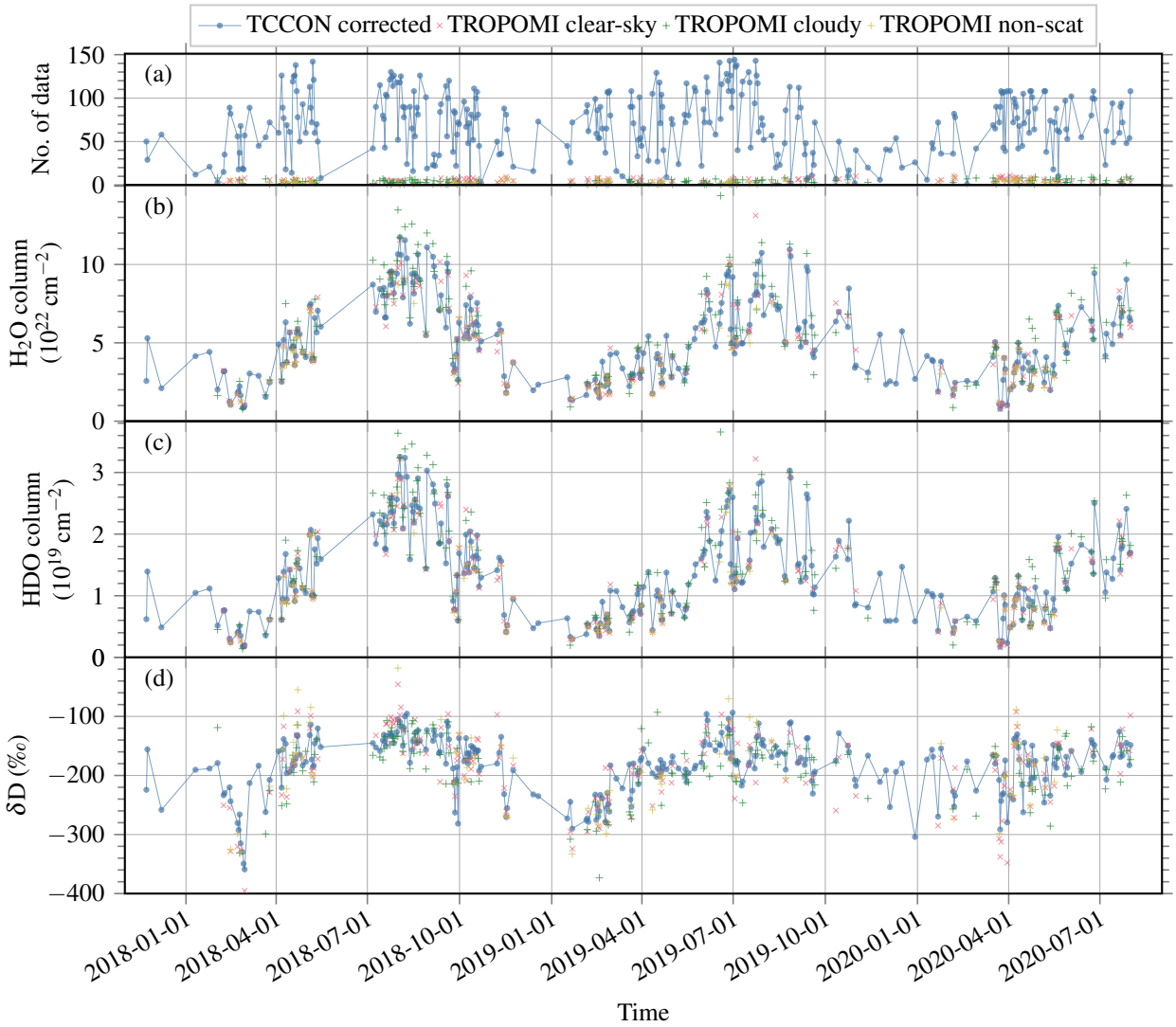

Figure 20: Time series of individual observations per day **(a)**, daily medians of H_2O columns **(b)**, HDO columns **(c)** and a posteriori δD **(d)** of corrected TCCON measurements (blue), TROPOMI clear-sky scenes (red), TROPOMI cloudy scenes (green), and the TROPOMI non-scattering retrieval (orange) at Karlsruhe, Germany (49.1° N, 8.4° E, 110 m a. a. l.)

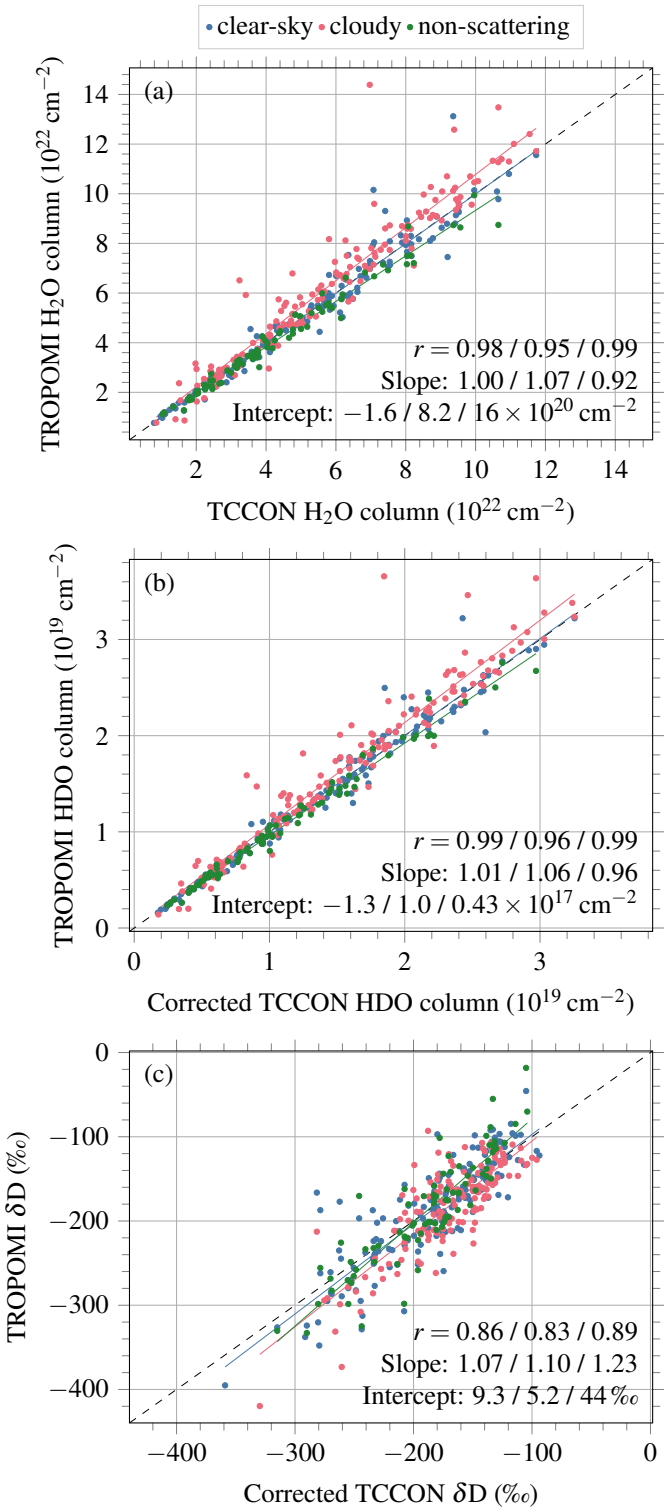

Figure 21: Correlations of TROPOMI observations against corrected TCCON measurements of H_2O columns **(a)**, HDO columns **(b)** and a posteriori δD **(c)** at Karlsruhe.

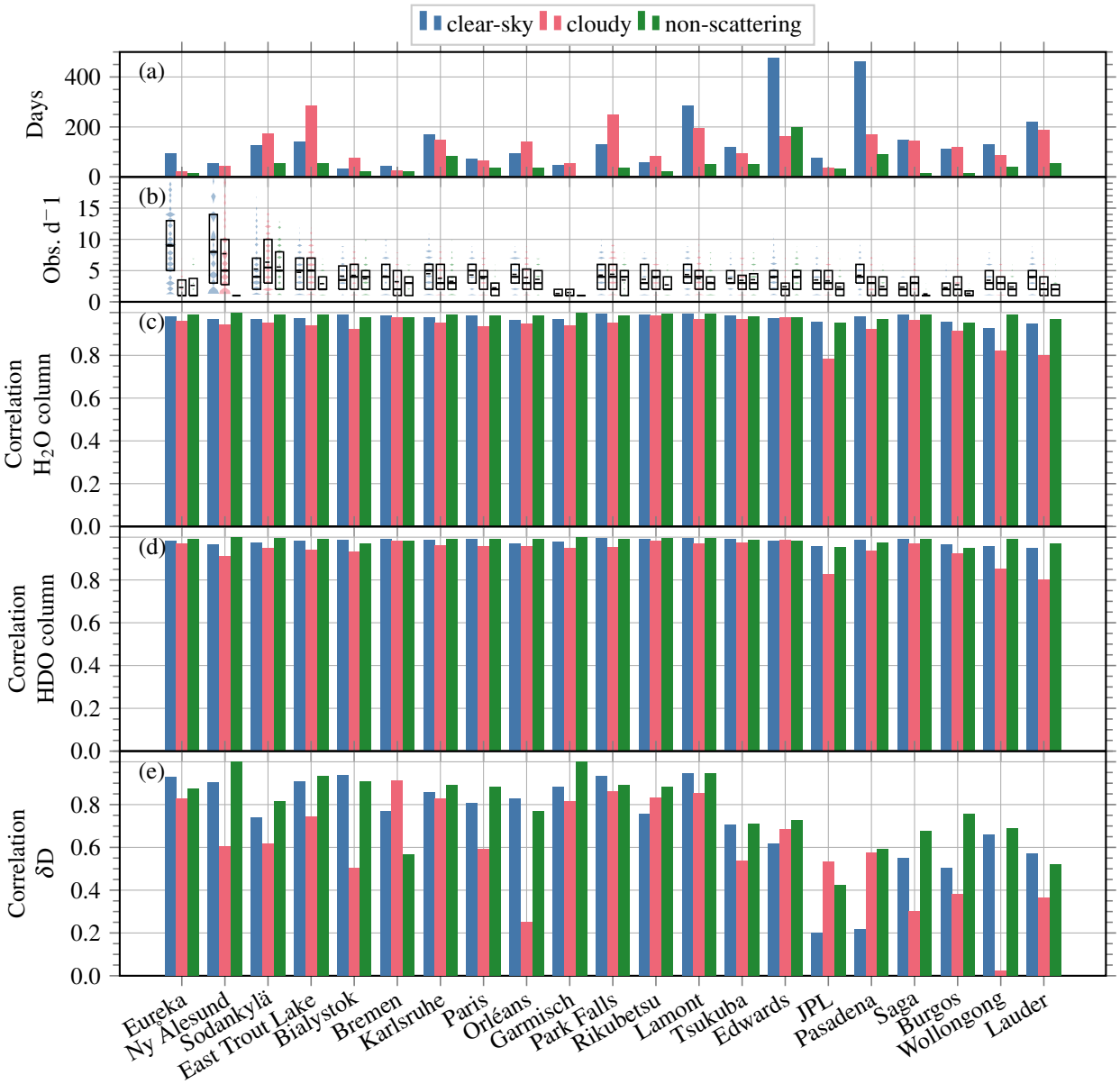

Figure 22: Number of days with observations **(a)**, observations per day **(b)**, correlation coefficients of H_2O columns **(c)**, correlation coefficients of HDO columns **(d)**, and correlation coefficients of a posteriori δD **(e)**.

cloud parameters retrieved in the pre-fit (see Tab. 4). The number of observations (ground pixels) per day (Fig. 22b) is usually around 4 but significantly higher at high latitudes due to multiple overpasses per day. Cloudy scenes encounter typically less observations per day compared to clear-sky scenes with a median of 3.4 vs. 4.1. The non-scattering retrieval has a significantly lower data yield with a median of 2.7 collocated ground pixels per day. The distributions visualised by the violin plots show that there is quite some spread with some days with a high number of observations.

Correlations of daily medians of H_2O and HDO columns are excellent at all stations (Fig. 22c, d). In a posteriori δD, correlations are lower at some stations, typically ones with low seasonal variation (Fig. 22e). For clear-sky scenes, correlation coefficients are similar to those of the non-scattering product except for δD at some stations like JPL and Pasadena. For cloudy scenes, the correlations are mostly slightly lower than for clear-sky scenes.

Biases are depicted in Fig. 23. At low and middle latitudes the bias is generally small: at these stations, the median for clear-sky scenes is 1.3×10^{21} cm^{-2} (1.8 %) in H_2O columns, 2.0×10^{16} cm^{-2} (-0.3 %) in HDO columns, and -8 ‰ (4.6 %) in δD, the one for cloudy scenes is 4.7×10^{21} cm^{-2} (8.8 %) in H_2O columns, 1.1×10^{18} cm^{-2} (6.5 %) in HDO columns, and -20 ‰ (12 %) in δD. High-latitude stations mostly have larger biases that can be as high as 20 % in the columns and 40 ‰ in a posteriori δD. The median bias at high latitude stations (Eureka, Ny Ålesund, Sodankylä, and East Trout Lake) in H_2O, HDO and δD is for clear-sky scenes 2.3×10^{21} cm^{-2} (9.5 %), 4.0×10^{17} cm^{-2} (0.4 %) and -37 ‰ (13 %) and for cloudy scenes 5.1×10^{21} cm^{-2} (12 %), 1.0×10^{18} cm^{-2} (9.1 %) and -24 ‰ (8.4 %), respectively. These high biases are similar, but partly more pronounced than for the non-scattering retrieval. High-latitude locations employ difficult measurement geometries with typically high solar zenith angles and low surface albedos, in which the additional estimation of cloud parameters seems to be even more challenging. In summer, these biases are typically lower than in darker seasons with higher solar zenith angles. The bias is also high at Garmisch, which lies in a mountainous region meaning a typically complex topography with large variation in surface altitude and albedo within a ground pixel. The median bias of all stations is for clear-sky scenes 1.4×10^{21} cm^{-2} (2.9 %) in H_2O columns, 1.1×10^{17} cm^{-2} (-0.3 %) in HDO columns, and -17 ‰ (9.9 %) in a posteriori δD. For cloudy scenes, it is 4.9×10^{21} cm^{-2} (11 %) in H_2O, 1.1×10^{17} cm^{-2} (7.9 %) in HDO, and -20 ‰ (9.7 %) in a posteriori δD. Although the absolute bias in δD is higher for cloudy scenes than for clear-sky scenes, the relative bias is not. This is connected to different conditions in cloudy and clear-sky weather. The distributions of the differences (TROPOMI – TCCON, visualised by the violin plots in Fig. 23) vary considerably between stations. Outliers are present, which shows that statistics over an adequate amount of data is needed for interpretation. Altogether, the performance of the new scattering retrieval for clear-sky scenes is similar to the one of the non-scattering retrieval, even though the scattering retrieval yields much more data. Biases are slightly smaller in HDO but slightly larger in a posteriori δD.

For a direct comparison of the new scattering retrieval to the non-scattering retrieval, only ground pixels for which both retrievals yield valid data are considered. The distributions of the differences (TROPOMI – TCCON) is very similar at most stations, with significant differences only at the coastal stations Burgos and Wollongong and at Park Falls. The station-to-station median bias for this scene selection at low and middle latitude stations is in H_2O 4.4×10^{20} cm^{-2} or 0.3 % for the scattering retrieval vs. -4.2×10^{18} cm^{-2} or 0.4 % for the non-scattering retrieval and in HDO -4.5×10^{16} cm^{-2} or -1.1 % vs. -9.3×10^{16} cm^{-2} or -1.3 %. In a posteriori δD it is -14 ‰ (7.5 %) for the scattering retrieval vs. -11 ‰ (5.4 %) for the non-scattering retrieval. This demonstrates that the performance of both retrievals is comparable.

3.4.5 Validation at high-altitude stations

Ground stations on high mountains (listed in Tab. 8) are special because the station height and the mean surface altitude of collocated satellite ground pixels typically differ considerably, which means that different air columns are observed by both. This leads to high biases if not accounted for. Therefore, the chosen prior plays an important role in this situation. To demonstrate the role of the prior in potential corrections, an additional run with HDO prior profiles obtained by an assumed more realistic δD profile as described in Sec. 3.2.1 has been performed. During the collocation, the same ground pixels are considered for both runs. Moreover, averaging kernels are not applied for this analysis because the prior profiles of the retrieval are used for the altitude correction.

The left column of Fig. 24 demonstrates the high biases of uncorrected clear-sky observations near Zugspitze (2964 m a. s. l.), which for the standard prior amount to 185 % in H_2O, 232 % in HDO and 75 ‰ in δD. Nevertheless, the time series does follow the relative variability of the reference.

The ground station on top of the mountain is always higher than the (mean) ground pixel altitude. To correct for

Table 8: List of high-altitude ground stations.

Station	Latitude	Longitude	Altitude	Data available from/to	Reference
Zugspitze	47.4° N	11.0° E	2960 m	24 Apr 2015 – 17 Oct 2019	Sussmann and Rettinger [2018b]
Izaña	28.3° N	16.5° W	2370 m	18 May 2007 – 31 Jul 2020	Blumenstock et al. [2017]

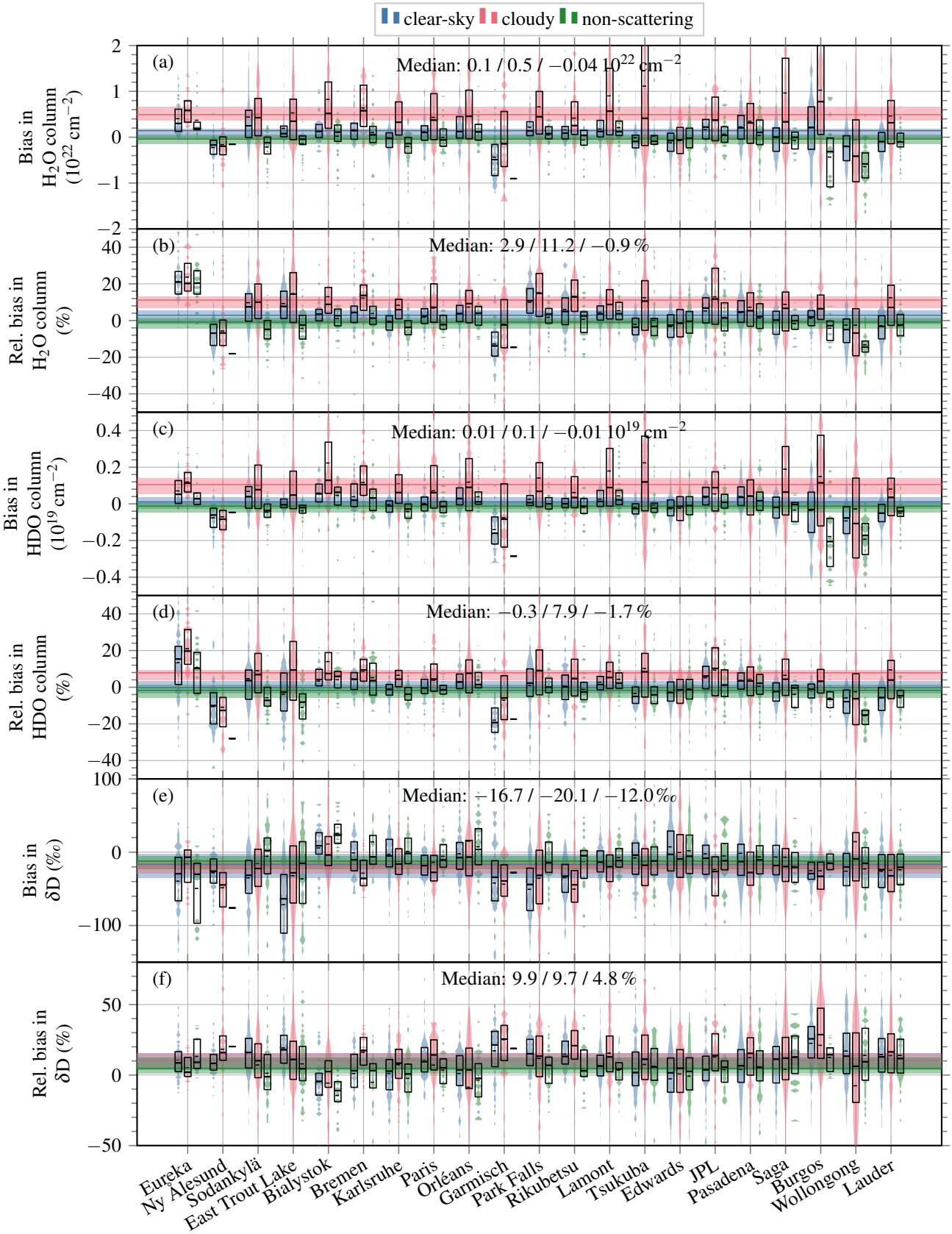

Figure 23: Bias in H_2O columns **(a)**, relative bias in H_2O columns **(b)**, bias in HDO columns **(c)**, relative bias in HDO columns **(d)**, bias in δD **(e)**, relative bias in δD **(f)** for clear-sky scenes (blue), cloudy scenes (red) and the non-scattering retrieval (green). The violin plots visualise the distributions of differences between TROPOMI and TCCON, the boxplots mark quartiles and the dashed lines inside the boxes the mean. Coloured horizontal lines denote station-to-station medians and the shading around them the station-to-station quartiles.

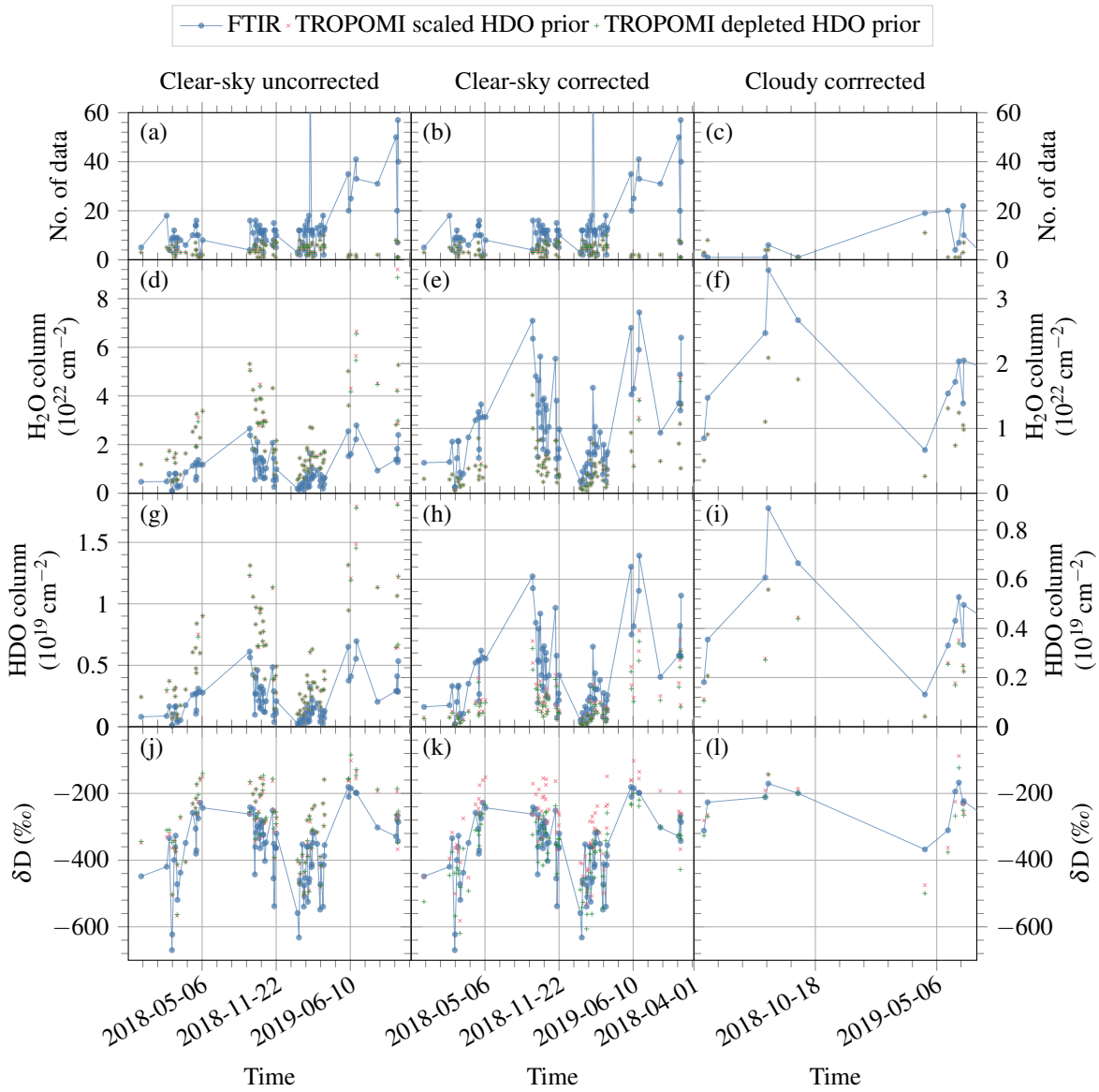

Figure 24: Time series of the amount of individual measurements per day near (first row), bias is H_2O column (second row), bias in HDO column (third row) and bias in δD (fourth row) at the high-altitude station Zugspitze (2964 m a. s. l.). The left panels **(a)**, **(d)**, **(g)** and **(j)** show clear-sky measurements without altitude correction; the centre panels **(b)**, **(e)**, **(h)** and **(k)** show the same measurements with altitude correction; and the right panels **(c)**, **(f)**, **(i)** and **(l)** show observations over optically thick clouds within an altitude range 1000 m above and 500 m below the station height. Please note that in the left panels the H_2O and HDO axes are different than in the centre and right panels, as indicated by the axis ticks.

the altitude differences, the partial columns of the TROPOMI observations above the station height are considered by truncating the scaled profile of the retrieval at the altitude of the station. This is the same procedure applied by Schneider et al. [2018, Sec. 4]. The second column of Fig. 24 depicts the resulting time series. The bias in both H_2O and HDO is greatly reduced to $-54\,\%$ and $-48\,\%$ for the standard prior and $-55\,\%$ and $-54\,\%$ for the depleted prior. In a posteriori δD a large difference between both priors is visible: while the bias for the scaled prior is practically the same as for the uncorrected case, 73 ‰, it is largely reduced to 4 ‰ for the depleted prior. The first is due to the fact that the altitude correction in H_2O and HDO cancels out when dividing HDO by H_2O if the same profile shapes are used. On the other hand, the small bias in δD in the second case shows that the assumed depleted HDO profile shape is indeed a good estimate for this case.

Another possibility is to utilise the shielding of clouds. To this end, scenes with optically thick clouds at an altitude similar to the station height as specified in Tab. 9 are selected. In these cases, the satellite measurement is sensitive above the cloud but insensitive below the cloud. Figure 25 illustrates the corresponding averaging kernels for a clear-sky and a cloudy scene. Since the FTIR has to see the sun and thus can measure only through gaps in the clouds or when the cloud cover changes within the collocation time, the amount of data for cloudy scenes is very small. Thus, the collocation radius is extended to $r_{90^\circ} = 50\,\mathrm{km}$ in this case. The inferred columns are corrected for the altitude difference between ground pixel and station height as described above. The right panel of Fig. 24 depicts the resulting time series. The biases in the columns and in a posteriori δD are acceptable for both priors. They amount to 4 ‰ for the scaled prior and -24 ‰ for the depleted prior. That the shielding yields good agreement with the scaled prior shows that the data provides information about the vertical distribution.

Figure 26 depicts biases for both high-altitude stations Zugspitze and Izaña. It confirms the behaviour seen in the time series at Zugspitze for both stations. Uncorrected clear-sky observations yield a large bias in all quantities. The altitude correction greatly reduces the bias in the H_2O and HDO columns. In δD, the correction cancels out when assuming the same vertical distributions of H_2O and HDO so that the bias remains. However, the altitude correction with a more realistic prior yields a substantial reduction of the bias in δD. For cloudy scenes with optically thick clouds in similar altitudes than the station height, the biases are also relatively small, although the validation is hampered by a small amount of data.

Table 9: Filter criteria for cloudy-sky scenes at high-altitude stations. Here h_s denotes the height of the ground site.

Quantity	Filter
Filter for cloudy scenes	
Cloud height	$h_s - 500\,\mathrm{m} \leq h_{cld} \leq h_s + 1000\,\mathrm{m}$
Cloud optical thickness	$\tau_{cld} \geq 2$

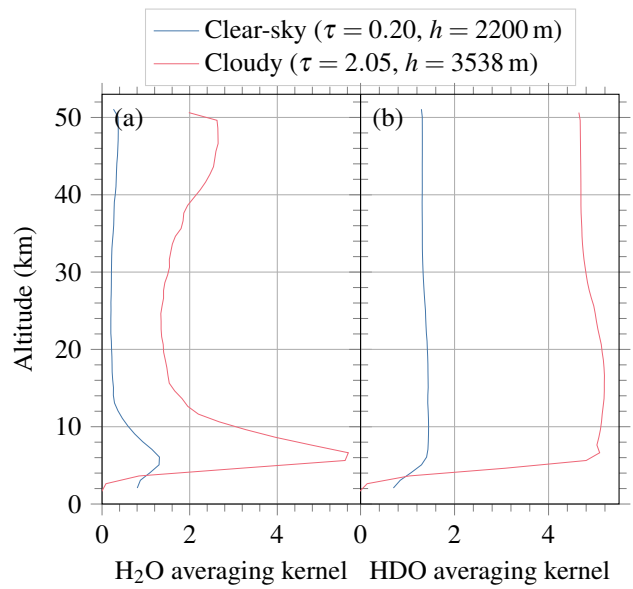

Figure 25: Averaging kernels of H_2O **(a)** and HDO **(b)** for a clear-sky scene (orbit 4725 on 11 Sep 2018, blue) and a cloudy scene (orbit 4839 on 19 Sep 2018, red) near Zugspitze

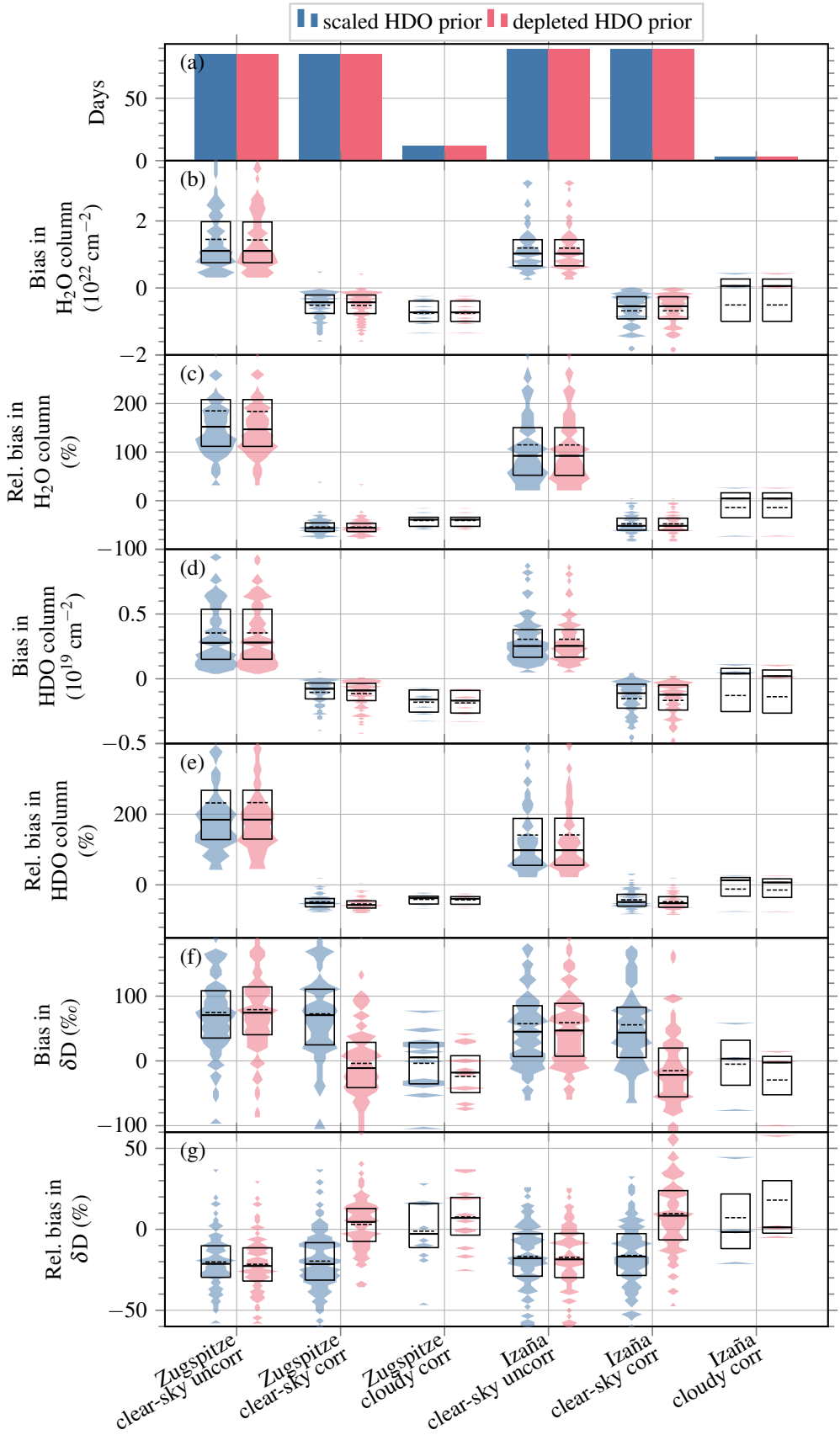

Figure 26: Biases for high-altitude TCCON stations plotted similarly as in Fig. 23, but for retrievals with the standard scaled HDO prior profile (blue) and a HDO prior profile obtained by assuming a more realistic δD profile described in Sec. 3.2.7. Shown are **(a)** the number of days with observations, **(b)** the bias in H_2O columns, **(c)** the relative bias in H_2O columns, **(d)** the bias in HDO columns, **(e)** the relative bias in HDO columns, **(f)** the bias in δD, and **(g)** the relative bias in δD. For each station, three entries are shown which correspond to uncorrected clear-sky observations, clear-sky observations corrected for the station altitude and altitude-corrected cloudy observations.

3.4.6 Global picture of the scattering retrieval

Figure 27 demonstrates a global picture of the new data set with a monthly average for September 2018. The most prominent improvement compared to the plot of the non-scattering product shown in Fig. 18 (Sec. 3.4.3) is a huge enhancement in data coverage, most prominently over the oceans and in regions at low latitudes with persistent clouds (e. g. over the Amazon, Central Africa and Oceania), where the non-scattering retrieval yields no data. Near these regions and also over northern India, δD is lower than in the clear-sky only data product which is attributed to different weather conditions at cloudy days compared to clear-sky days.

In the spatial distribution of column integrated H_2O and δD shown in Fig. 27 the major characteristic features of the atmospheric water cycle and the isotopic effects as described by Dansgaard [1964] can be recognised. In Fig. 27a, a very moist intertropical band can be distinguished. The typically deep convective clouds associated with the moistest band shield most of the scenes in the area of the intertropical convergence zone (Equatorial Atlantic, and Pacific, see Fig. 27c). This might lead to a slight underestimation of the total column δD in this area. The moist continental regions associated with the northern hemisphere's fading summer monsoon systems (West African Monsoon, southeast Asian Monsoon) show relatively more depleted δD total columns (see coastal West Africa, China) compared to other regions in the same latitudinal band (see subtropical oceans, India and North Africa). The combined (H_2O, δD) information is likely to provide more insight into mixing and cloud and below cloud evaporation effects in these regions [Noone, 2012].

The subtropical ocean regions are all associated with relatively high total column δD except for spots with distinctly

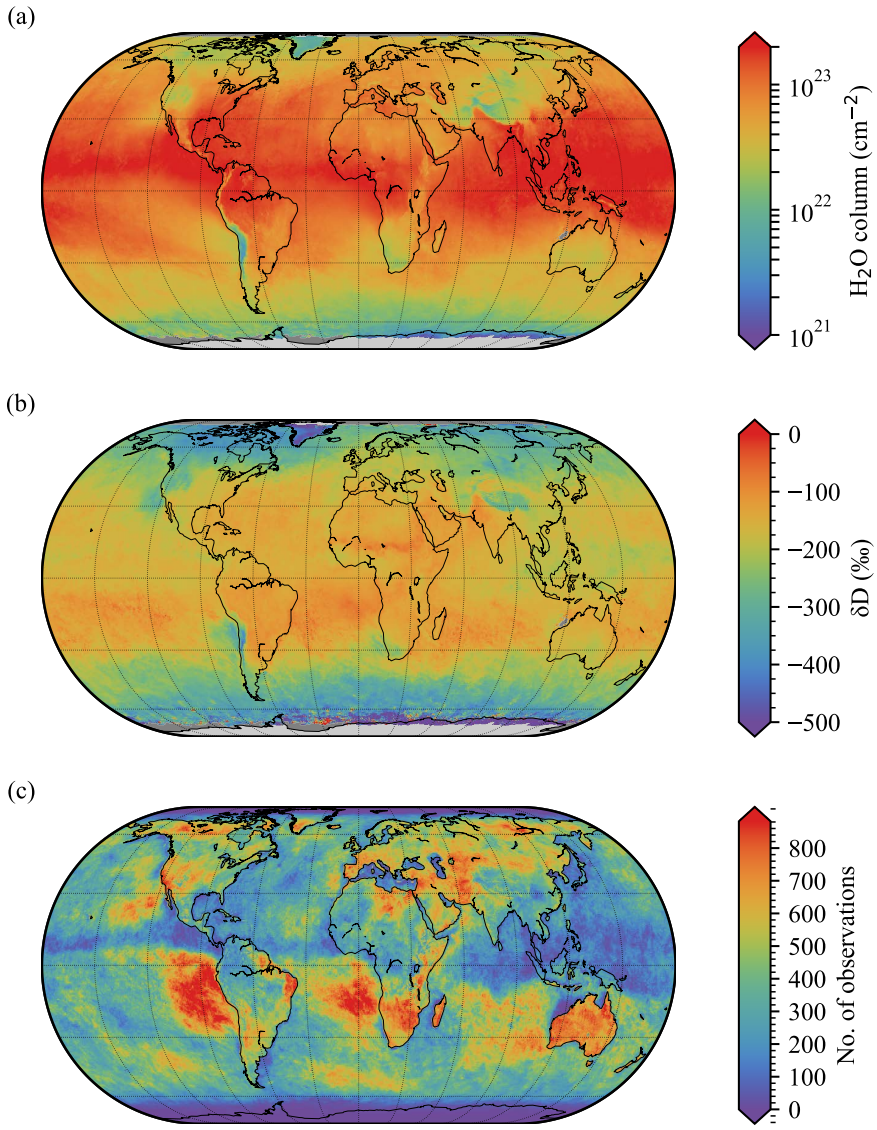

Figure 27: Global plots of **(a)** number of observations, **(b)** average H_2O and **(b)** average δD for September 2018 on a $0.5° \times 0.5°$ grid. The average of δD is weighted with the H_2O column.

lower values found along the eastern coasts of the ocean basins. In the latter coastal regions around 30° N/S stratocumulus capped areas with strong inversions are prominent and enhanced subsidence is frequently observed [Norris, 1998, Myers and Norris, 2013], which probably leads to the distinct local minima in total column δD and total column H_2O.

In the regions of frequent occurrence of extratropical cyclones (storm tracks) over the midlatitude western North Atlantic, western North Pacific and in the Southern Ocean, sharp gradients can be observed in total column δD. The equatorward flanks of the storm tracks are associated with warm air and total column δD of about -100‰. In contrast, much lower values of about -300‰ can be observed on the subpolar flanks of the storm tracks. In these regions the frequent occurrence of extratropical cyclones [Wernli and Schwierz, 2006] strongly modulate the variability of δD signals of atmospheric water vapour [Thurnherr et al., 2020b]. In the Southern Ocean, the spatial pattern of oceanic total column δD reflects the spiral shaped winding of the Southern Ocean storm track around Antarctica with more frequent storms in the central South Atlantic compared to the Central South Pacific. In the latter region a tongue of more enriched total column δD reaches far South towards the Antarctic coast.

Along the Antarctic coast, the very low total column δD might be due to cold air outbreaks or strong katabatic outflows at low levels, advecting very depleted Antarctic water vapour over the ocean [Thurnherr et al., 2020b]. However, the data availability over these coastal Antarctic region is very limited (Fig. 27c). A comparison with high resolution isotope-enabled numerical model simulations in these regions as well as in very high altitude mountainous regions, would certainly help in ruling out important biases due to uncertainties associated with the retrieval in these regions with complex topography and small-scale variations in the albedo.

The data coverage, as can bee seen on the example for the month of September 2018 in Fig. 27c, is highly variable in space. Particularly over tropical oceanic regions, the data is very sparse due to shielding by high clouds. Over high latitude land regions, the data is also sparse due to high solar zenith angles and low surface albedos (recall the SZA filter and albedo filter, cf. Tab. 4). In contrast, particularly in regions of enhanced subsidence in the subtropics a large number of observations are available. A weak seasonal cycle in the amount of observations exists particularly at high latitudes.

3.4.7 Case study using the scattering retrieval

Figure 28 demonstrates single overpass results over the North Atlantic Ocean. On 17 January 2020 a cold air outbreak forms along the North American east coast, behind a cold front associated with a North Atlantic cyclone. The cold front can be identified in Fig. 28a by the quasi-zonal cloudy band, marked by a strong gradient of low to high total column H_2O between 15° N and 25° N across the front. The cold air mass (see low values of potential temperature at 850 hPa behind the cold front in Fig. 28f) travels southward towards the tropics between 17 and 20 January 2020 (Figs. 28–30). The cold, subsiding air behind the cold front is very dry (Fig. 28a) and is associated with low total column δD values between -400 and -200‰ (Fig. 28b) which are characteristic of the cold sector of extratropical cyclones [Thurnherr et al., 2020a]. Marine cold air outbreak clouds are typically low level clouds with high cloud fraction (stratocumulus, cumulus, Fig. 28e) and moderate optical thickness [Fig. 28c, Fletcher et al., 2016]. The very high δD values of $\sim$0‰ stretching in a bow from $\sim$20° N, 40° W westward are caused by low sensitivity in low altitudes due to cloud shielding. These sensitivity issues are reflected by very low values of the column averaging kernel (Fig. 28d). The magnitude of the null-space error is determined by the deviation of the shape of the prior profile to the real profile. The prior depends on time and location, thus the null-space error may be different in different regions. Nevertheless, these data still contain valuable information that can be interpreted in combination with measurements or model simulations providing vertical profiles of H_2O and HDO that can be combined with the vertical sensitivity of the satellite retrievals.

The analysis of successive overpasses between 18 and 20 January (Fig. 29, 28, 30) shows a rapid moistening of the originally very dry and depleted cold air mass. When it leaves the North American continent on 18 January the cold sector air has total column δD of less than -400‰. On 20 January, when the cold front reaches into the tropics, the δD of the cold sector is in the range -300 to -200‰. The dry and cold air subsiding above the boundary layer typically induces large humidity gradients near the ocean surface and consequently leads to enhanced surface evaporation fluxes that favour a rapid moistening and continuous increase in δD of cold sector air as it travels southward [Aemisegger and Papritz, 2018]. The δD in Fig. 28b shows large spatial variability in the cold sector hinting towards different degrees of vertical mixing in different regions of the cold sector, most likely due to variations in subsidence strength. The latter aspect could be investigated in more detail using this dataset in combination with a numerical weather model including isotopes.

This variability in δD at low total column H_2O can also be observed when displaying the cold sector data in a (H_2O, δD) phase space (Fig. 31). In contrast to the cold air mass behind the cold front, the trade wind air mass in front of the cold front is associated with very high total column δD (Fig. 31b). Reduced subsidence and stronger shallow convective activity with deeper clouds are the reason for the higher δD on the warm, trade wind side of the front (see also Aemisegger et al. [2020] for a discussion on the impact of extratropical intrusions behind cold fronts on the low-level δD signals in the tropics).

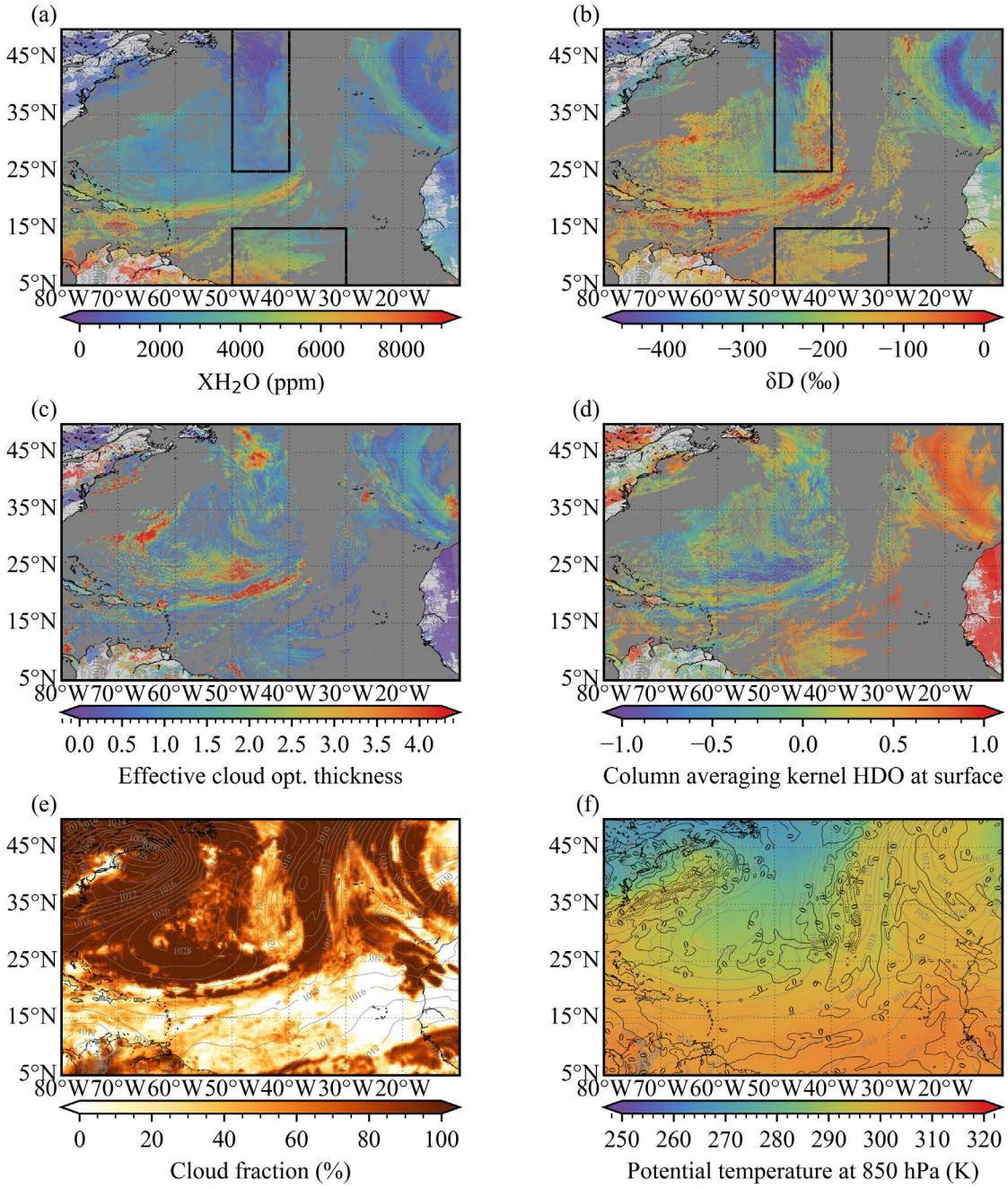

Figure 28: TROPOMI single overpass results of XH_2O **(a)**, δD **(b)**, retrieved effective cloud optical thickness **(c)** and column averaging kernel at the surface **(d)** over the North Atlantic on 19 Jan 2020; ERA5 cloud fraction **(e)** and ERA5 potential temperatures at 850 hPa at 15:00 UTC **(d)**. The grey contours in all panels show ERA5 mean sea-level pressure at 15:00 UTC with a contour line distance of 2 hPa. The black contours in (f) show vertical winds at 500 hPa in levels of 0.5 Pa s^{-1}. The boxes in (a) and (b) mark the regions for which Rayleigh plots are depicted in Fig. 31.

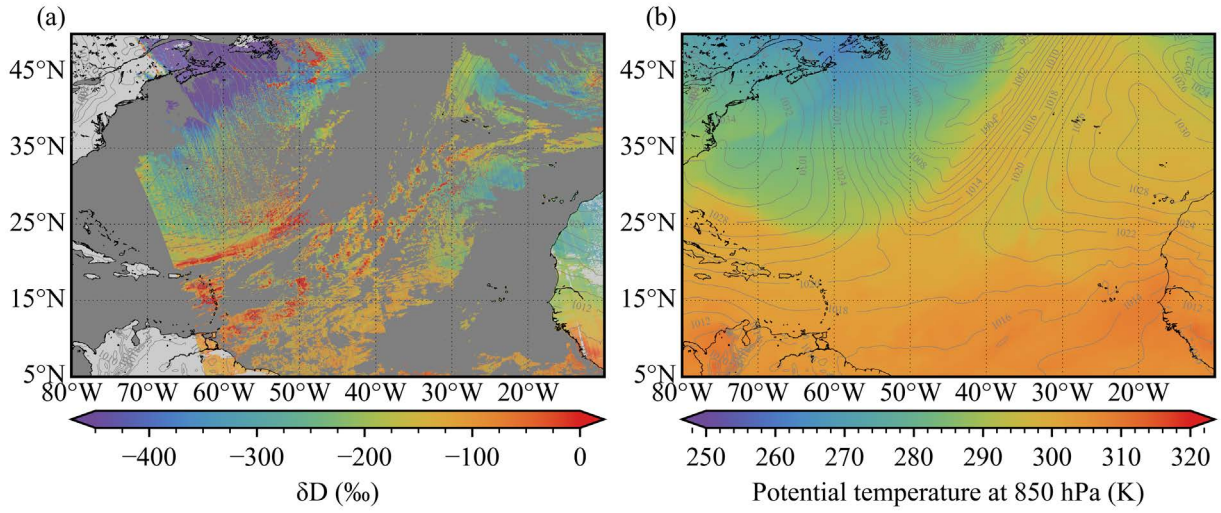

Figure 29: TROPOMI single overpass δD **(a)** and ERA5 potential temperatures at 850 hPa at 15:00 UTC **(b)** on 18 Jan 2020. The grey contours in all panels show ERA5 mean sea-level pressure at 15:00 UTC with a contour line distance of 2 hPa.

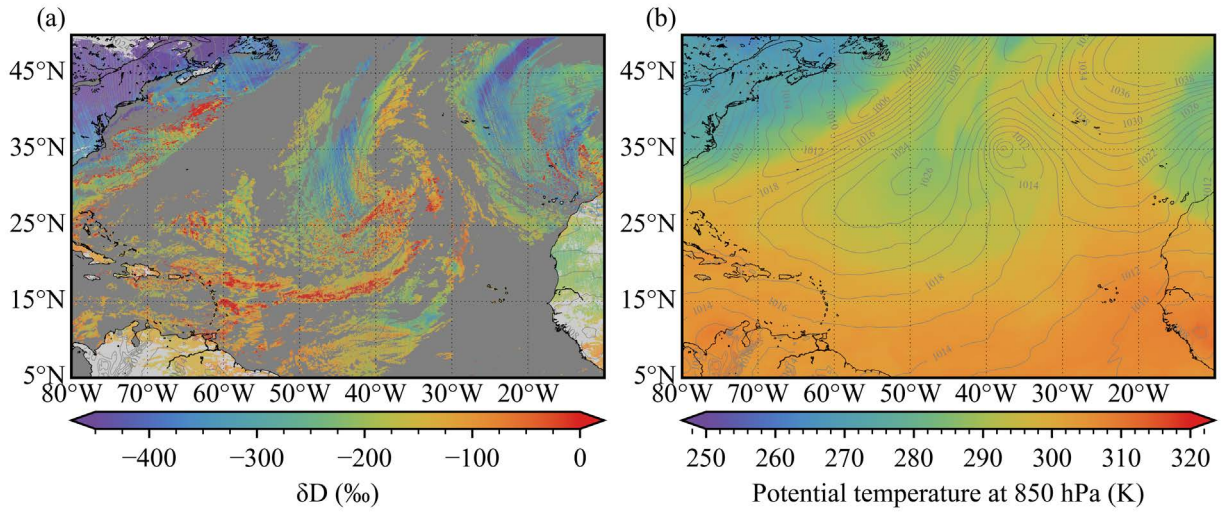

Figure 30: TROPOMI single overpass δD **(a)** and ERA5 potential temperatures at 850 hPa at 15:00 UTC **(b)** on 20 Jan 2020. The grey contours in all panels show ERA5 mean sea-level pressure at 15:00 UTC with a contour line distance of 2 hPa.

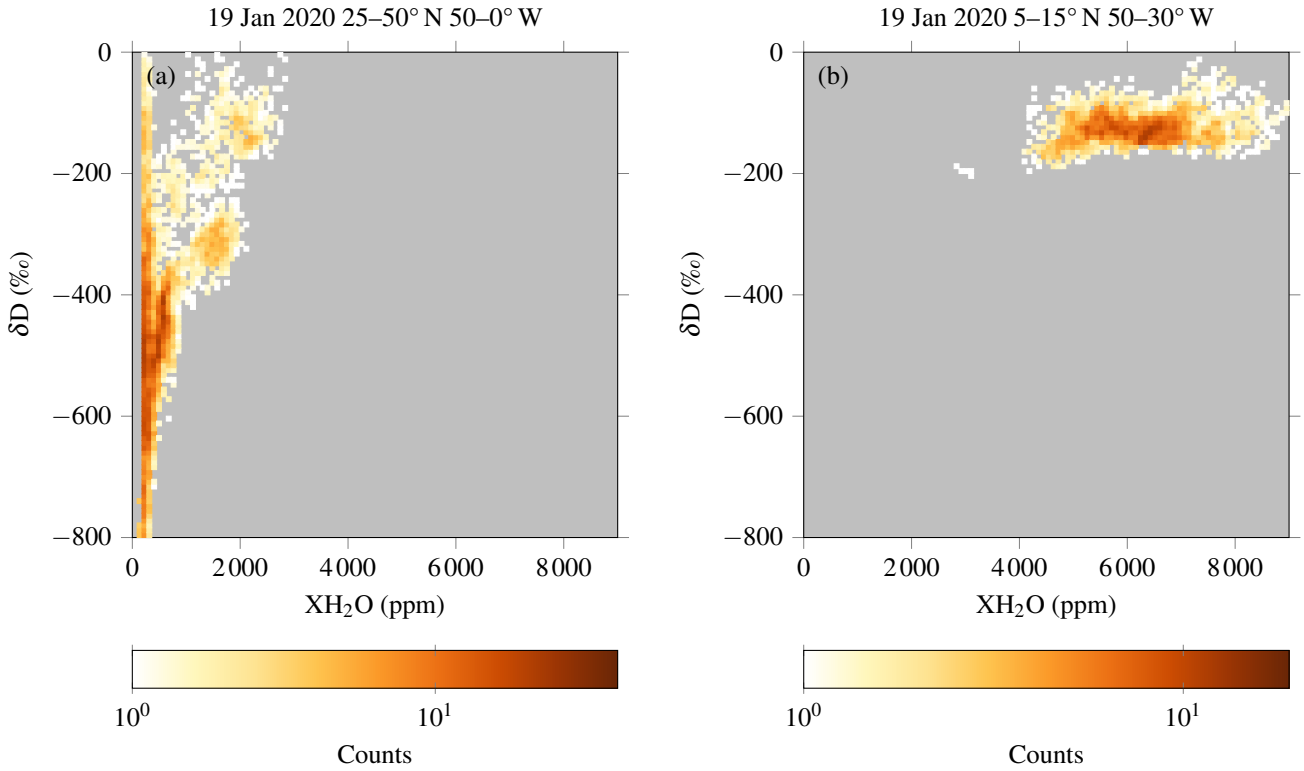

Figure 31: Histograms of TROPOMI observations on 19 Jan 2020 **(a)** in the area 25–50° N, 50–0° W comprising the cold sector and **(b)** in the area 5–15° N, 50–30° W containing the cold front.

In future comparisons of TROPOMI all-sky observations with vertical profiles from aircraft-based measurement campaigns will be helpful for identifying potentially remaining biases in very dry compared to very moist conditions. Furthermore, studies combining TROPOMI data with high resolution numerical modelling will provide a promising data basis for studying the interaction between the moist boundary layer and the subsiding dry free tropospheric air, which is key in determining the variability in the low-level cloud cover properties.

4 Conclusions and Recommendations

Two new data products from TROPOMI have been developed within this fellowship: first a clear-sky data product of H_2O and HDO columns using a forward model which ignores scattering (non-scattering retrieval), and a second a data product for cloudy and clear-sky scenes which provides retrieved effective cloud parameters additionally to the H_2O and HDO columns (scattering retrieval).

The validation has been hindered by a bias in the TCCON reference data due to a missing calibration and a lack of other recent reference data, however a correction for the bias has been derived by scaling TCCON HDO so that TCCON a posteriori δD matches MUSICA-NDACC δD for the period where data from both are available. Later, recent MUSICA-NDACC data for three stations have become available. These are inhomogeneous to TCCON, as not only HDO, but also H_2O are different. That has been fixed by scaling MUSICA H_2O to match TCCON H_2O and scaling MUSICA HDO by the same factor to preserve MUSICA δD.

The performance of the retrievals is good. The non-scattering product has a station-to-station mean bias of $(-0.3 \pm 1) \times 10^{21}$ molec cm^{-2} or (-0.7 ± 3.5) % in H_2O, $(-0.9 \pm 3) \times 10^{17}$ molec cm^{-2} or (-1.3 ± 3.3) % in HDO, and (-7 ± 13) ‰ or (3.8 ± 6.5) % in a posteriori δD

The development of the product for cloudy scenes happened to be much more difficult than anticipated. After many experiments it has turned out that the approach of the CO product [Landgraf et al., 2016], which comprises fitting effective cloud parameters simultaneous to the trace gases in its spectral range 2315–2338 nm, cannot directly be transferred to the spectral window 2354–2380.5 nm because it introduces errors in the inferred water vapour columns, maybe due to interferences and/or inaccuracies of the methane spectroscopy in the latter window. Thus, the effective cloud parameters are determined in a pre-fit in the spectral window from 2310 nm to 2338 nm where large absorption features of methane not interfering with water vapour are present. The resulting parameters are taken over to the final fit in the spectral

window from 2354.0 nm to 2380.5 nm, where they are fixed while the trace gases are fitted. This neglects the spectral dependence of the cloud optical thickness in the spectral range between 2310 nm and 2380 nm.

The scattering product tremendously improves data coverage compared to the non-scattering retrieval, not only due to additional scenes with low clouds which particularly also enable retrievals over oceans, but also due to less restrictive filtering for clear-sky scenes. Nevertheless, data quality is good with a mean bias for clear-sky scenes of $(0.9 \pm 2) \times 10^{21}$ molec cm^{-2} or (-2.0 ± 5.1) % in H_2O, $(0.7 \pm 4) \times 10^{17}$ molec cm^{-2} or (0.1 ± 3.9) % in HDO, and (-15 ± 16) ‰ or (8.5 ± 6.7) % in a posteriori δD. The mean bias for cloudy scenes is $(3 \pm 3) \times 10^{21}$ molec cm^{-2} or (7.9 ± 6.4) % in H_2O, $(6 \pm 7) \times 10^{17}$ molec cm^{-2} or (4.9 ± 5.4) % in HDO, and (-20 ± 11) ‰ or (10 ± 5.7) % in a posteriori δD.

Retrievals over clouds allow to infer information of the vertical distribution of H_2O and HDO due to shielding. This has been shown at high-altitude TCCON stations. Here, an altitude correction is necessary because the satellite and the ground station on top of the mountain observe different partial columns. Taking the partial column of the satellite observation above the ground station height eliminates biases in H_2O and HDO columns, however for clear-sky scenes the bias in a posteriori δD remains since the correction cancels due to the same prior profile shapes for H_2O and HDO. Considering scenes with clouds in an altitude similar to the ground station height eliminates this bias utilising the shielding of the clouds. The bias in a posteriori δD can also be eliminated by using more realistic prior profile shapes.

For each data set, a case study with single overpass results has been performed in collaboration with Franziska Aemisegger (ETH Zürich). The use of the non-scattering retrieval is demonstrated by examining an atmospheric blocking event over northeastern Europe on 30 July 2018. Depleted air masses are found in the core of the anticyclone due to subsidence transporting upper tropospheric air towards lower levels. At the edge of the anticyclone a ring of enriched air is observed. The scattering retrieval is used to study a cold air outbreak in January 2020 over the Atlantic ocean. Retrievals from single overpasses of consecutive days nicely show the transport of depleted continental air from high to subtropical latitudes.

The retrieval performance above clouds can be further improved by optimising the regularisation of cloud parameters and surface albedo. To this end, a sensitivity study is necessary. The validation would benefit considerably by an improvement of the reference data. An ad hoc correction has been derived to eliminate a bias in TCCON HDO. Nevertheless, a proper calibration of the TCCON HDO product would be very important for proper validation of satellite products. Furthermore, a homogenisation of the TCCON and MUSICA-NDACC products would be valuable.

5 Publications

5.1 Peer-reviewed articles

Andreas Schneider, Tobias Borsdorff, Joost aan de Brugh, Franziska Aemisegger, Dietrich G. Feist, Rigel Kivi, Frank Hase, Matthias Schneider, and Jochen Landgraf. First data set of H_2O/HDO columns from the Tropospheric Monitoring Instrument (TROPOMI). *Atmos. Meas. Tech.*, 13(1):85–100, 2020. `https://dx.doi.org/10.5194/amt-13-85-2020`.

Andreas Schneider, Tobias Borsdorff, Joost aan de Brugh, Alba Lorente, Franziska Aemisegger, David Noone, Dean Henze, Rigel Kivi, and Jochen Landgraf. Retrieving H_2O/HDO columns over cloudy and clear-sky scenes from the Tropospheric Monitoring Instrument (TROPOMI). Submitted to *Atmos. Meas. Tech.*, 2021.

Conference contributions

Andreas Schneider, Tobias Borsdorff, Joost aan de Brugh, Manfred Birk, Georg Wagner and Jochen Landgraf. A new scientific data product of H_2O/HDO columns from TROPOMI 2.3 µm reflectance measurements. *EGU General Assembly*, Vienna, Austria, 8th April 2019.

Andreas Schneider, Tobias Borsdorff, Joost aan de Brugh, Franziska Aemisegger and Jochen Landgraf. (Towards) A New Scientific Data Product Of H_2O/HDO Vertical Columns From TROPOMI 2.3 µm Reflectance Measurements. *ESA Living Planet Symposium*, Milano, Italy, 13th May 2019.

Andreas Schneider, Tobias Borsdorff, Joost and aan de Brugh, Alba Lorente Delgado, Franziska Aemisegger and Jochen Landgraf. A new scientific data product of H_2O/HDO columns from TROPOMI's short-wave infrared band and validation against TCCON. *Copernicus Sentinel-5 Precursor validation team workshop*, Frascati, Italy, 11th–14th November 2019.

References

F. Aemisegger and L. Papritz. A climatology of strong large-scale ocean evaporation events. Part I: Identification, global distribution, and associated climate conditions. *J. Climate*, 31(18):7287–7312, 2018. doi: 10.1175/JCLI-D-17-0591.1.

F. Aemisegger, R. Vogel, P. Graf, F. Dahinden, L. Villiger, F. Jansen, S. Bony, B. Stevens, and H. Wernli. How rossby wave breaking modulates the water cycle in the north atlantic trade wind region. *Weather Clim. Dynam. Discuss.*, 2020:1–47, 2020. doi: 10.5194/wcd-2020-51. Accepted.

S. Barthlott, M. Schneider, F. Hase, T. Blumenstock, M. Kiel, D. Dubravica, O. E. García, E. Sepúlveda, G. Mengistu Tsidu, S. Takele Kenea, M. Grutter, E. F. Plaza-Medina, W. Stremme, K. Strong, D. Weaver, M. Palm, T. Warneke, J. Notholt, E. Mahieu, C. Servais, N. Jones, D. W. T. Griffith, D. Smale, and J. Robinson. Tropospheric water vapour isotopologue data ($H_2{}^{16}O$, $H_2{}^{18}O$, and $HD^{16}O$) as obtained from NDACC/FTIR solar absorption spectra. *Earth Syst. Sci. Data*, 9(1):15–29, 2017. doi: 10.5194/essd-9-15-2017.

T. Blumenstock, F. Hase, M. Schneider, O. E. García, and E. Sepúlveda. TCCON data from izaña (es), release ggg2014.r1, 2017.

T. Borsdorff, O. P. Hasekamp, A. Wassmann, and J. Landgraf. Insights into tikhonov regularization: application to trace gas column retrieval and the efficient calculation of total column averaging kernels. *Atmos. Meas. Tech.*, 7(2):523–535, 2014. doi: 10.5194/amt-7-523-2014.

Copernicus Climate Service. online, 2018. URL `https://climate.copernicus.eu/dry-and-warm-spring-and-summer`. vis 21 May 2019.

H. Craig. Isotopic variations in meteoric waters. *Science*, 133(3465):1702–1703, 1961a. doi: 10.1126/science.133.3465.1702.

H. Craig. Standard for reporting concentrations of deuterium and oxygen-18 in natural waters. *Science*, 133(3467):1833–1834, 1961b. doi: 10.1126/science.133.3467.1833.

W. Dansgaard. Stable isotopes in precipitation. *Tellus*, 16(4):436–468, 1964. doi: 10.3402/tellusa.v16i4.8993.

M. De Mazière, M. K. Sha, F. Desmet, C. Hermans, F. Scolas, N. Kumps, J.-M. Metzger, V. Duflot, and J.-P. Cammas. Tccon data from réunion island (re), release ggg2014.r1, 2017.

M. De Mazière, A. M. Thompson, M. J. Kurylo, J. D. Wild, G. Bernhard, T. Blumenstock, G. O. Braathen, J. W. Hannigan, J.-C. Lambert, T. Leblanc, T. J. McGee, G. Nedoluha, I. Petropavlovskikh, G. Seckmeyer, P. C. Simon, W. Steinbrecht, and S. E. Strahan. The network for the detection of atmospheric composition change (NDACC): history, status and perspectives. *Atmos. Chem. Phys.*, 18(7):4935–4964, 2018. doi: 10.5194/acp-18-4935-2018.

N. M. Deutscher, J. Notholt, J. Messerschmidt, C. Weinzierl, T. Warneke, C. Petri, and P. Grupe. Tccon data from bialystok (pl), release ggg2014.r2, 2019.

C. Dyroff, S. Sanati, E. Christner, A. Zahn, M. Balzer, H. Bouquet, J. B. McManus, Y. González-Ramos, and M. Schneider. Airborne in situ vertical profiling of HDO / $H_2{}^{16}O$ in the subtropical troposphere during the MUSICA remote sensing validation campaign. *Atmos. Meas. Tech.*, 8(5):2037–2049, 2015. doi: 10.5194/amt-8-2037-2015.

D. G. Feist, S. G. Arnold, N. John, and M. C. Geibel. Tccon data from ascension island (sh), release ggg2014.r0, 2014.

J. K. Fletcher, S. Mason, and C. Jakob. A climatology of clouds in marine cold air outbreaks in both hemispheres. *J. Climate*, 29(18):6677–6692, 2016. doi: 10.1175/JCLI-D-15-0783.1.

T.-Y. Goo, Y.-S. Oh, and V. A. Velazco. Tccon data from anmeyondo (kr), release ggg2014.r0, 2014.

I. Gordon, L. Rothman, C. Hill, R. Kochanov, Y. Tan, P. Bernath, M. Birk, V. Boudon, A. Campargue, K. Chance, B. Drouin, J.-M. Flaud, R. Gamache, J. Hodges, D. Jacquemart, V. Perevalov, A. Perrin, K. Shine, M.-A. Smith, J. Tennyson, G. Toon, H. Tran, V. Tyuterev, A. Barbe, A. Császár, V. Devi, T. Furtenbacher, J. Harrison, J.-M. Hartmann, A. Jolly, T. Johnson, T. Karman, I. Kleiner, A. Kyuberis, J. Loos, O. Lyulin, S. Massie, S. Mikhailenko, N. Moazzen-Ahmadi, H. Müller, O. Naumenko, A. Nikitin, O. Polyansky, M. Rey, M. Rotger, S. Sharpe, K. Sung, E. Starikova, S. Tashkun, J. V. Auwera, G. Wagner, J. Wilzewski, P. Wcisło, S. Yu, and E. Zak. The HITRAN2016 molecular spectroscopic database. *J. Quant. Spectrosc. Radiat. Transfer*, 203:3–69, 2017. doi: 10.1016/j.jqsrt.2017.06.038.

D. W. Griffith, N. M. Deutscher, V. A. Velazco, P. O. Wennberg, Y. Yavin, G. Keppel-Aleks, R. A. Washenfelder, G. C. Toon, J.-F. Blavier, C. Paton-Walsh, N. B. Jones, G. C. Kettlewell, B. J. Connor, R. C. Macatangay, C. Roehl, M. Ryczek, J. Glowacki, T. Culgan, and G. W. Bryant. Tccon data from darwin (au), release ggg2014.r0, 2014a.

D. W. Griffith, V. A. Velazco, N. M. Deutscher, C. Paton-Walsh, N. B. Jones, S. R. Wilson, R. C. Macatangay, G. C. Kettlewell, R. R. Buchholz, and M. O. Riggenbach. TCCON data from wollongong (au), release ggg2014.r0, 2014b.

S. Gubler, S. Scherrer, S. Bader, A. Burgstall, A. Casanueva, A. Duguay-Tetzlaff, R. Gehrig, S. Kotlarski, and C. Spirig. Hitze und Trockenheit im Sommerhalbjahr 2018 – eine klimatologische Übersicht. Fachbericht MeteoSchweiz 272, MeteoSchweiz, 2018. URL `https://www.meteoschweiz.admin.ch/content/dam/meteoswiss/de/service-und-publikationen/Publikationen/doc/Fachbericht_TrockenheitHitze_2018_final_d.pdf`. vis 7 Jun 2019.

R. Hagemann, G. Nief, and E. Roth. Absolute isotopic scale for deuterium analysis of natural waters. absolute D/H ratio for SMOW. *Tellus*, 22(6):712–715, 1970. doi: 10.3402/tellusa.v22i6.10278.

F. Hase, T. Blumenstock, S. Dohe, J. Groß, and M. Kiel. Tccon data from karlsruhe (de), release ggg2014.r1, 2015.

H. Hu, J. Landgraf, R. Detmers, T. Borsdorff, J. Aan de Brugh, I. Aben, A. Butz, and O. Hasekamp. Toward global mapping of methane with TROPOMI: First results and intersatellite comparison to GOSAT. *Geophys. Res. Lett.*, 45 (8):3682–3689, 2018. doi: 10.1002/2018GL077259.

L. T. Iraci, J. R. Podolske, P. W. Hillyard, C. Roehl, P. O. Wennberg, J.-F. Blavier, J. Landeros, N. Allen, D. Wunch, J. Zavaleta, E. Quigley, G. B. Osterman, R. Albertson, K. Dunwoody, and H. Boyden. Tccon data from edwards (us), release ggg2014.r1, 2016.

S. Kawakami, H. Ohyama, K. Arai, H. Okumura, C. Taura, T. Fukamachi, and M. Sakashita. Tccon data from saga (jp), release ggg2014.r0, 2014.

R. Kivi, P. Heikkinen, and E. Kyrö. Tccon data from sodankylä (fi), release ggg2014.r0, 2014.

M. Krol, S. Houweling, B. Bregman, M. van den Broek, A. Segers, P. van Velthoven, W. Peters, F. Dentener, and P. Bergamaschi. The two-way nested global chemistry-transport zoom model TM5: algorithm and applications. *Atmos. Chem. Phys.*, 5(2):417–432, 2005. doi: 10.5194/acp-5-417-2005.

J. Landgraf, J. aan de Brugh, R. Scheepmaker, T. Borsdorff, H. Hu, S. Houweling, A. Butz, I. Aben, and O. Hasekamp. Carbon monoxide total column retrievals from TROPOMI shortwave infrared measurements. *Atmos. Meas. Tech.*, 9 (10):4955–4975, 2016. doi: 10.5194/amt-9-4955-2016.

A. Ludewig, Q. Kleipool, R. Bartstra, R. Landzaat, J. Leloux, E. Loots, P. Meijering, E. van der Plas, N. Rozemeijer, F. Vonk, and P. Veefkind. In-flight calibration results of the TROPOMI payload on board the sentinel-5 precursor satellite. *Atmos. Meas. Tech.*, 13(7):3561–3580, 2020. doi: 10.5194/amt-13-3561-2020.

I. Morino, T. Matsuzaki, and M. Horikawa. Tccon data from tsukuba (jp), 125hr, release ggg2014.r2, 2018a.

I. Morino, V. A. Velazco, A. Hori, O. Uchino, and D. W. Griffith. Tccon data from burgos, ilocos norte (ph), release ggg2014.r0, 2018b.

I. Morino, N. Yokozeki, T. Matsuzaki, and M. Horikawa. Tccon data from rikubetsu (jp), release ggg2014.r2, 2018c.

T. A. Myers and J. R. Norris. Observational evidence that enhanced subsidence reduces subtropical marine boundary layer cloudiness. *J. Climate*, 26(19):7507–7524, 2013. doi: 10.1175/JCLI-D-12-00736.1.

D. Noone. Pairing measurements of the water vapor isotope ratio with humidity to deduce atmospheric moistening and dehydration in the tropical midtroposphere. *J. Climate*, 25(13):4476–4494, 2012. doi: 10.1175/JCLI-D-11-00582.1.

J. R. Norris. Low cloud type over the ocean from surface observations. part i: Relationship to surface meteorology and the vertical distribution of temperature and moisture. *J. Climate*, 11(3):369–382, 1998. doi: 10.1175/1520-0442(1998)011<0369:LCTOTO>2.0.CO;2.

J. Notholt, C. Petri, T. Warneke, N. M. Deutscher, M. Palm, M. Buschmann, C. Weinzierl, R. C. Macatangay, and P. Grupe. TCCON data from bremen (de), release ggg2014.r1, 2019a.

J. Notholt, T. Warneke, C. Petri, N. M. Deutscher, C. Weinzierl, M. Palm, and M. Buschmann. TCCON data from ny ålesund, spitsbergen (no), release ggg2014.r1, 2019b.

S. Pfahl and H. Wernli. Quantifying the relevance of atmospheric blocking for co-located temperature extremes in the northern hemisphere on (sub-)daily time scales. *Geophysical Research Letters*, 39(12), 2012. doi: 10.1029/2012GL052261.

D. F. Pollard, J. Robinson, and H. Shiona. Tccon data from lauder (nz), release ggg2014.r0, 2019.

M. Rast, J. Johannessen, and W. Mauser. Review of understanding of earth's hydrological cycle: Observations, theory and modelling. *Surv. Geophys.*, 35(3):491–513, 2014. doi: 10.1007/s10712-014-9279-x.

C. D. Rodgers. *Inverse methods for atmospheric sounding: theory and practice*, volume 2 of *Series on atmospheric, oceanic and planetary physics*. World Scientific, Singapore, 2000. ISBN 981-022740-X.

L. Rothman, I. Gordon, A. Barbe, D. Benner, P. Bernath, M. Birk, V. Boudon, L. Brown, A. Campargue, J.-P. Champion, K. Chance, L. Coudert, V. Dana, V. Devi, S. Fally, J.-M. Flaud, R. Gamache, A. Goldman, D. Jacquemart, I. Kleiner, N. Lacome, W. Lafferty, J.-Y. Mandin, S. Massie, S. Mikhailenko, C. Miller, N. Moazzen-Ahmadi, O. Naumenko, A. Nikitin, J. Orphal, V. Perevalov, A. Perrin, A. Predoi-Cross, C. Rinsland, M. Rotger, M. Šimečková, M. Smith, K. Sung, S. Tashkun, J. Tennyson, R. Toth, A. Vandaele, and J. V. Auwera. The HITRAN 2008 molecular spectroscopic database. *J. Quant. Spectrosc. Radiat. Transfer*, 110(9):533–572, 2009. doi: https://doi.org/10.1016/j.jqsrt.2009.02.013.

R. A. Scheepmaker, C. Frankenberg, A. Galli, A. Butz, H. Schrijver, N. M. Deutscher, D. Wunch, T. Warneke, S. Fally, and I. Aben. Improved water vapour spectroscopy in the 4174–4300 cm^{-1} region and its impact on SCIAMACHY HDO/H_2O measurements. *Atmos. Meas. Tech.*, 6(4):879–894, 2013. doi: 10.5194/amt-6-879-2013.

R. A. Scheepmaker, J. aan de Brugh, H. Hu, T. Borsdorff, C. Frankenberg, C. Risi, O. Hasekamp, I. Aben, and J. Landgraf. HDO and H_2O total column retrievals from TROPOMI shortwave infrared measurements. *Atmos. Meas. Tech.*, 9(8): 3921–3937, 2016. doi: 10.5194/amt-9-3921-2016.

A. Schneider, T. Borsdorff, J. aan de Brugh, H. Hu, and J. Landgraf. A full-mission data set of H_2O and HDO columns from SCIAMACHY 2.3 µm reflectance measurements. *Atmos. Meas. Tech.*, 11(6):3339–3350, 2018. doi: 10.5194/amt-11-3339-2018.

M. Schneider, Y. González, C. Dyroff, E. Christner, A. Wiegele, S. Barthlott, O. E. García, E. Sepúlveda, F. Hase, J. Andrey, T. Blumenstock, C. Guirado, R. Ramos, and S. Rodríguez. Empirical validation and proof of added value of MUSICA's tropospheric {H_2O,δD} remote sensing products. *Atmos. Meas. Tech.*, 8(1):483–503, 2015. doi: 10.5194/amt-8-483-2015.

M. Schneider, A. Wiegele, S. Barthlott, Y. González, E. Christner, C. Dyroff, O. E. García, F. Hase, T. Blumenstock, E. Sepúlveda, G. Mengistu Tsidu, S. Takele Kenea, S. Rodríguez, and J. Andrey. Accomplishments of the MUSICA project to provide accurate, long-term, global and high-resolution observations of tropospheric {H_2O,δD} pairs – a review. *Atmos. Meas. Tech.*, 9(7):2845–2875, 2016. doi: 10.5194/amt-9-2845-2016.

V. Sherlock, B. Connor, J. Robinson, H. Shiona, D. Smale, and D. F. Pollard. TCCON data from lauder (nz), 125hr, release ggg2014.r0, 2014.

R. Siddans. S5P-NPP cloud processor ATBD. Technical report, Rutherford Appleton Laboratory, 2016. URL `http://www.tropomi.eu/sites/default/files/files/S5P-NPPC-RAL-ATBD-0001_NPP-Clouds_v1p0p0_20160212.pdf`.

B. Stevens and S. Bony. What are climate models missing? *Science*, 340(6136):1053–1054, 2013. doi: 10.1126/science.1237554.

K. Strong, S. Roche, J. E. Franklin, J. Mendonca, E. Lutsch, D. Weaver, P. F. Fogal, J. R. Drummond, R. Batchelor, and R. Lindenmaier. TCCON data from eureka (ca), release ggg2014.r3, 2019.

R. Sussmann and M. Rettinger. Tccon data from garmisch (de), release ggg2014.r2, 2018a.

R. Sussmann and M. Rettinger. Tccon data from zugspitze (de), release ggg2014.r1, 2018b.

I. Thurnherr, K. Hartmuth, L. Jansing, J. Gehring, M. Boettcher, I. Gorodetskaya, M. Werner, H. Wernli, and F. Aemisegger. The role of air–sea fluxes for the water vapour isotope signals in the cold and warm sectors of extratropical cyclones over the southern ocean. *Weather Clim. Dynam. Discuss.*, 2020:1–42, 2020a. doi: 10.5194/wcd-2020-46. Under review.

I. Thurnherr, A. Kozachek, P. Graf, Y. Weng, D. Bolshiyanov, S. Landwehr, S. Pfahl, J. Schmale, H. Sodemann, H. C. Steen-Larsen, A. Toffoli, H. Wernli, and F. Aemisegger. Meridional and vertical variations of the water vapour isotopic composition in the marine boundary layer over the atlantic and southern ocean. *Atmos. Chem. Phys.*, 20(9):5811–5835, 2020b. doi: 10.5194/acp-20-5811-2020.

R. M. Trigo, I. F. Trigo, C. C. DaCamara, and T. J. Osborn. Climate impact of the european winter blocking episodes from the NCEP/NCAR reanalyses. *Climate Dyn.*, 23:17–28, 2004. doi: 10.1007/s00382-004-0410-4.

Y. Té, P. Jeseck, and C. Janssen. Tccon data from paris (fr), release ggg2014.r0, 2014.

R. M. van Hees, P. J. J. Tol, S. Cadot, M. Krijger, S. T. Persijn, T. A. van Kempen, R. Snel, I. Aben, and R. W. M. Hoogeveen. Determination of the TROPOMI-SWIR instrument spectral response function. *Atmos. Meas. Tech.*, 11 (7):3917–3933, 2018. doi: 10.5194/amt-11-3917-2018.

T. Warneke, J. Messerschmidt, J. Notholt, C. Weinzierl, N. M. Deutscher, C. Petri, and P. Grupe. Tccon data from orléans (fr), release ggg2014.r1, 2019.

P. O. Wennberg, D. Wunch, C. M. Roehl, J.-F. Blavier, G. C. Toon, and N. T. Allen. Tccon data from caltech (us), release ggg2014.r1, 2015.

P. O. Wennberg, C. M. Roehl, J.-F. Blavier, D. Wunch, and N. T. Allen. Tccon data from jet propulsion laboratory (us), 2011, release ggg2014.r1, 2016a.

P. O. Wennberg, D. Wunch, C. M. Roehl, J.-F. Blavier, G. C. Toon, and N. T. Allen. Tccon data from lamont (us), release ggg2014.r1, 2016b.

P. O. Wennberg, C. M. Roehl, D. Wunch, G. C. Toon, J.-F. Blavier, R. Washenfelder, G. Keppel-Aleks, N. T. Allen, and J. Ayers. Tccon data from park falls (us), release ggg2014.r1, 2017.

H. Wernli and C. Schwierz. Surface cyclones in the era-40 dataset (1958–2001). part i: Novel identification method and global climatology. *J. Atmos. Sci.*, 63(10):2486–2507, 2006. doi: 10.1175/JAS3766.1.

D. Wunch, G. C. Toon, J.-F. L. Blavier, R. A. Washenfelder, J. Notholt, B. J. Connor, D. W. T. Griffith, V. Sherlock, and P. O. Wennberg. The total carbon column observing network. *Philos. T. Roy. Soc. A*, 369(1943):2087–2112, 2011. doi: 10.1098/rsta.2010.0240.

D. Wunch, G. C. Toon, V. Sherlock, N. M. Deutscher, C. Liu, D. G. Feist, and P. O. Wennberg. The total carbon column observing network's GGG2014 data version. Technical report, TCCON, 2015.

D. Wunch, J. Mendonca, O. Colebatch, N. T. Allen, J.-F. Blavier, S. Roche, J. Hedelius, G. Neufeld, S. Springett, D. Worthy, R. Kessler, and K. Strong. Tccon data from east trout lake, sk (ca), release ggg2014.r1, 2018.

W. G. Zdunkowski, R. M. Welch, and G. Korb. An investigation of the structure of typical two-stream-methods for the calculation of solar fluxes and heating rates in clouds. *Contrib. Atmos. Phys.*, 53(2):147–166, 1980.